

A deep learning framework for efficient pathology image analysis

Peter Neidlinger (1), Tim Lenz (1), Sebastian Foersch (2), Chiara M. L. Loeffler (1, 3, 4), Jan Clusmann (1, 5), Marco Gustav (1), Lawrence A. Shaktah (1), Rupert Langer (6), Bastian Dislich (7), Lisa A. Boardman (8), Amy J. French (9), Ellen L. Goode (10), Andrea Gsur (11), Stefanie Brezina (11), Marc J. Gunter (12, 13), Robert Steinfelder (14), Hans-Michael Behrens (15), Christoph Röcken (15), Tabitha Harrison (14, 16), Ulrike Peters (14, 16), Amanda I. Phipps (14, 16), Giuseppe Curigliano (17, 18), Nicola Fusco (18, 19), Antonio Marra (17), Michael Hoffmeister (20), Hermann Brenner (20, 21), Jakob Nikolas Kather+ (1, 3, 22)

+ Correspondence to jakob-nikolas.kather@alumni.dkfz.de

1. Else Kroener Fresenius Center for Digital Health, Faculty of Medicine and University Hospital Carl Gustav Carus, TUD Dresden University of Technology, 01307 Dresden, Germany
2. Institute of Pathology, University Medical Center Mainz, Mainz, Germany
3. Department of Medicine I, Faculty of Medicine and University Hospital Carl Gustav Carus, TUD Dresden University of Technology, 01307 Dresden, Germany
4. National Center for Tumor Diseases Dresden (NCT/UCC), a partnership between DKFZ, Faculty of Medicine and University Hospital Carl Gustav Carus, TUD Dresden University of Technology, and Helmholtz-Zentrum Dresden - Rossendorf (HZDR), Dresden, Germany
5. Department of Medicine III, University Hospital RWTH Aachen, Aachen, Germany
6. Institute of Pathology and Molecular Pathology, Kepler University Hospital, Johannes Kepler University Linz, Linz, Austria
7. Institute of Tissue Medicine and Pathology, University of Bern, Bern, Switzerland
8. Division of Gastroenterology and Hepatology, Mayo Clinic, Rochester, Minnesota, USA.
9. Division of Laboratory Genetics, Department of Laboratory Medicine and Pathology, Mayo Clinic, Rochester, Minnesota, USA.
10. Department of Quantitative Health Sciences, Division of Epidemiology, Mayo Clinic, Rochester, Minnesota, USA.
11. Center for Cancer Research, Medical University of Vienna, Vienna, Austria.
12. Nutrition and Metabolism Branch, International Agency for Research on Cancer, World Health Organization, Lyon, France.
13. Cancer Epidemiology and Prevention Research Unit, School of Public Health, Imperial College London, London, United Kingdom.
14. Division of Public Health Sciences, Fred Hutchinson Cancer Center, Seattle, WA, USA.
15. Department of Pathology, University Hospital Schleswig-Holstein, Kiel, Germany
16. Department of Epidemiology, University of Washington, Seattle, WA, USA.
17. Division of New Drugs and Early Drug Development, European Institute of Oncology IRCCS, Milan, Italy
18. Department of Oncology and Hemato-Oncology, University of Milan, Italy
19. Division of Pathology, European Institute of Oncology IRCCS, Milan, Italy
20. Division of Clinical Epidemiology and Aging Research, German Cancer Research Center (DKFZ), Heidelberg, Germany
21. German Cancer Consortium (DKTK), German Cancer Research Center (DKFZ), Heidelberg, Germany
22. Medical Oncology, National Center for Tumor Diseases (NCT), University Hospital Heidelberg, Heidelberg, Germany

Abstract

Artificial intelligence (AI) has transformed digital pathology by enabling biomarker prediction from high-resolution whole slide images (WSIs). However, current methods are computationally inefficient, processing thousands of redundant tiles per WSI and requiring complex aggregator models. We introduce EAGLE (Efficient Approach for Guided Local Examination), a deep learning framework that emulates pathologists by selectively analyzing informative regions. EAGLE incorporates two foundation models: CHIEF for efficient tile selection and Virchow2 for extracting high-quality features. Benchmarking was conducted against leading slide- and tile-level foundation models across 31 tasks from four cancer types, spanning morphology, biomarker prediction and prognosis. EAGLE outperformed state-of-the-art foundation models by up to 23% and achieved the highest AUROC overall. It processed a slide in 2.27 seconds, reducing computational time by more than 99% compared to existing models. This efficiency enables real-time workflows, allows pathologists to validate all tiles which are used by the model during analysis, and eliminates dependence on high-performance computing, making AI-powered pathology more accessible. By reliably identifying meaningful regions and minimizing artifacts, EAGLE provides robust and interpretable outputs, supporting rapid slide searches, integration into multi-omics pipelines and emerging clinical foundation models.

Main

Artificial intelligence (AI) has significantly advanced computational pathology (CPath) by enabling the extraction of clinically relevant information from gigapixel-scale whole slide images (WSIs)¹⁻⁶. Existing methods use resource-intensive vision transformers trained with self-supervised learning to encode detailed morphological features essential for diagnosis, prognosis, and treatment planning in oncology⁷⁻¹¹. While these approaches have shown great promise across a wide range of tasks, their inefficiencies and limited scalability highlight the need for solutions that better align with real-world diagnostic workflows. Recently, pathology-specific multimodal large language models (MLLMs) have emerged as AI copilots for clinical decision-making, but they often underperform in biomarker prediction and the regulatory pathway for approving such models as medical devices remains uncertain¹²⁻¹⁶.

Current methods predominantly operate at the tile level, requiring the extraction and analysis of thousands of tiles per WSI, with datasets in this study averaging approximately 18,000 tiles per slide at a resolution of 0.5 $\mu\text{m}/\text{pixel}$ (MPP). This computationally intensive process deviates from how pathologists evaluate slides, as they selectively focus on regions of interest¹⁷⁻¹⁹. Moreover, tile-wise features are aggregated into slide-level predictions using models

trained separately for each task, limiting scalability and interpretability^{8,20,21}. The complexity of these models often obscures the decision-making process, making it challenging to understand how predictions are derived and which tissue regions are influential. These systems also struggle in data-scarce scenarios, where tile selection often fails to identify the most relevant regions, leading to suboptimal predictions²². Such scenarios are often a clinical reality, for example during the evaluation of small biopsy specimens.

To address these limitations, we developed EAGLE (Efficient Approach for Guided Local Examination), a framework that emulates the diagnostic strategy of pathologists by focusing on a small, informative subset of tiles within WSIs. EAGLE combines CHIEF, for global tissue representation and guided tile selection, with Virchow2, for detailed feature extraction from selected tiles. This combination drastically reduces computational demands while increasing performance^{23,24} (**Figure 1a-c**). By selecting clinically meaningful tiles, EAGLE enhances interpretability and scalability, particularly in biomarker prediction tasks where subtle morphological features are critical²⁵. Unlike MLLMs, which emphasize multimodal interaction, EAGLE prioritizes efficient high-quality WSI analysis. Still, it can integrate with MLLMs to provide valuable inputs for enhanced contextual analysis. Through comprehensive evaluation against state-of-the-art models, including multiple instance learning (MIL) and slide-encoder approaches, we demonstrate the efficacy and robustness of EAGLE across 31 tasks spanning four cancer types^{8-10,23,24,26-30}.

Results

EAGLE improves upon state-of-the-art approaches

We benchmarked EAGLE against state-of-the-art slide-encoder and tile-encoder approaches, covering 31 tasks across breast (BRCA), colorectal (CRC), gastric (STAD), and non-small cell lung cancers (NSCLC), as well as three key task categories: morphology, biomarker, and prognosis. The slide-encoder models included TITAN²⁸, COBRA³⁰, CHIEF²³, Prism²⁶, MADELEINE²⁷, and Prov-GigaPath⁹; the tile encoders or foundation models (Virchow2²⁴, CONCH v1.5²⁸, CONCH²⁹, Prov-GigaPath⁹, CTransPath⁸, Virchow¹⁰) were aggregated utilizing attention-based multiple instance learning (ABMIL)²¹, the standardized pipeline STAMP¹⁸, or simply by averaging all embeddings. All classifiers were trained using a five-fold cross-validation setup on The Cancer Genome Atlas (TCGA) data, resulting in five models per task. Each model was then evaluated on the full external test cohorts (CPTAC, DACHS, Kiel, Bern, IEO), ensuring external validation without data leakage.

Across all 31 tasks, EAGLE and TITAN achieved the highest average area under the receiver operating characteristic curve (AUROC) scores of 0.742 and 0.740, respectively. Following were Virchow2 in STAMP (0.723) and CONCH v1.5 in STAMP (0.721), suggesting that modern slide encoders often outperform strong tile-level baselines (**Figure 1c,2a,S1a**). EAGLE exceeded key AUROC thresholds more often than other models, surpassing 0.800 in 39% of tasks and 0.650 in 77% of tasks—higher than TITAN (35% and 68%) and Virchow2 (26% and 65%) (**Figure 2b**). Looking at task-specific performance, EAGLE (0.772), TITAN (0.763), and COBRA (0.757) excelled on biomarker tasks, which predict molecular alterations or protein expression. In morphology tasks, which classify tumor location or histological patterns, TITAN achieved the highest performance (0.814), followed by Virchow2 (0.785) and EAGLE (0.782). Tile-level CONCH v1.5 in STAMP (0.648) held an advantage in prognosis, which assesses tumor spread, with EAGLE achieving the highest prognosis performance among slide encoders (0.630) (**Figure 2c,S2**). EAGLE also scored highest in three of the four cancer types—BRCA (0.737), CRC (0.710), and STAD (0.755)—while TITAN scored highest in lung (0.810) (**Figure S3**). Beyond AUROC, EAGLE achieved the highest average area under the precision-recall curve (AUPRC) scores (0.566), followed by COBRA (0.556). In balanced accuracy, EAGLE and TITAN performed best with average scores of 0.657 and 0.655, respectively. TITAN held the highest average F1 scores (0.498), followed by EAGLE (0.490) (**Figure S1b-d**).

We assessed the statistical significance of AUROC differences with two-sided DeLong’s tests, controlling the false discovery rate using the Benjamini–Hochberg procedure. For each patient, predictions from the five cross-validation models were averaged to yield a single score. Under these ensemble conditions, EAGLE achieved an average AUROC of 0.750, followed by TITAN (0.744) and CONCH (0.736) (**Figure S4a**). EAGLE often significantly outperformed alternative approaches, particularly in DACHS CRC tasks (MSI, *BRAF*, *KRAS*, M-Status, and N-Status), potentially due to the large cohort size, which provided increased statistical power. In DACHS *BRAF* mutation prediction, EAGLE statistically outperformed all models except COBRA (**Figure S4b**).

These findings highlight EAGLE as one of the leading models across multiple evaluation metrics (AUROC, AUPRC, balanced accuracy, and F1), excelling particularly in biomarker prediction. It further maintains strong, generalizable performance across diverse tasks, cancer types, and external cohorts.

Ablation Studies

To understand which design choices yield EAGLE’s performance gains, we conducted extensive ablation studies. First, we compared two approaches for representing whole slides: one that uses a specialized slide encoder and one that averages the features from all individual image tiles of a

patient. For most architectures, the slide-encoder approach surpassed an average of tile embeddings. EAGLE (0.742) outperformed both Virchow2 (0.720) and CTransPath (0.632) mean tile embeddings. However, Prov-GigaPath Slide Encoder (0.628) fell below the mean of Prov-GigaPath tile embeddings (0.666) (**Figure S5a**). Second, we investigated the optimal number of tiles required for EAGLE to maximize predictive performance. Using CHIEF to rank tiles by relevance at 2 MPP resolution, we extracted features from the top 5, 10, 25, 50, and 100 tiles and evaluated their impact on AUROC. Selecting 25 tiles yielded the highest AUROC (0.745), suggesting that a limited but carefully chosen subset is sufficient to capture essential morphological features. Notably, even using just 5 tiles (0.727) outperformed averaging all available tiles (0.720), highlighting that filtering out less informative regions enhances performance (**Figure S5b**). We also compared simple averaging to CHIEF's attention-weighted aggregation across these subsets. While results varied slightly depending on tile count, performance at 25 tiles remained identical (0.745 vs. 0.744). Given this, we opted for equal weighting of the top 25 tiles, balancing efficiency and interpretability (**Figure S5b**). We then compared two methods for creating a patient-level representation: Most existing works average slide embeddings to obtain one patient vector. Alternatively, we aggregated all slides of a patient in a single slide encoder run, which improved performance, as shown in TITAN (0.733 vs. 0.740) and Prov-GigaPath (0.610 vs. 0.628) (**Figure S5c**). We further explored different tile aggregation methods for tile-encoder baselines at 1.14 MPP (STAMP, ABMIL, mean). Here, STAMP scored highest in four of five models, ABMIL ranked second in three, and mean embeddings placed last in four. An exception was Virchow2, where STAMP (0.709) and mean embeddings (0.708) performed almost identically, both surpassing ABMIL (0.698) (**Figure S5d**). Next, we examined how magnification choices influence performance. While EAGLE and COBRA each peaked at 2 MPP (0.742 and 0.719, respectively), TITAN and Prism favored 0.5 MPP (0.740 and 0.695). For Prov-GigaPath (0.628), CHIEF (0.684) and MADELEINE (0.672), 1.14 MPP worked best, implying that the optimal resolution differs between models (**Figure S5e**). Finally, we substituted Virchow2 within the EAGLE framework with alternative tile encoders. Despite some performance drop, several replacements outperformed the corresponding slide-encoder baselines. For example, Prov-GigaPath EAGLE reached an AUROC of 0.702 compared to 0.628 for the Prov-GigaPath slide encoder. Similarly, CTransPath EAGLE (0.693) outperformed CHIEF (0.684) and CONCH EAGLE (0.701) surpassed MADELEINE (0.672) (**Figure S5f**).

Together, these investigations highlight that careful tile selection, slide-level encoding, and optimal magnification are pivotal for high accuracy, and that combining a lightweight tile encoder for global scanning with a stronger encoder on selected regions confers a marked advantage.

Efficiency and Performance in Data-Scarce Scenarios

We next quantified computational requirements for the major pipeline steps, measuring average inference times for tile extraction and slide encoding using 25 representative slides of the benchmarking dataset (**Figure 3a**). All measurements were performed on a workstation equipped with an L40 GPU (48GB), considering only model inference times. The slowest step is the tile-level feature extraction. On average, CTransPath at 0.5 MPP required 25.4 s/WSI and only 2.01 s/WSI at 2 MPP. By contrast, CONCH v1.5 at 0.5 MPP cost 191.85 s/WSI, and Prov-GigaPath 16 min/WSI (**Table S1**). The faster slide encoding took on average 0.36 ms for CHIEF (2 MPP), while TITAN (0.5 MPP) took 3296 ms and Prism (0.5 MPP) 153 ms. EAGLE first processed each WSI with CTransPath at 2 MPP (2.01 s/WSI), applied CHIEF (0.36 ms/WSIs), and selected 25 key tiles. Those tiles were then re-extracted with Virchow2 (0.26 s/WSI). On average, ~2% of tiles are reprocessed in detail at 2 MPP using Virchow2 (or ~0.1% at 0.5 MPP). When plotted against overall AUROC, EAGLE obtained the highest performance while ranking among the most efficient in terms of run time and floating point operations (FLOPs) (**Figure 3b,c,d**). Prov-GigaPath, in contrast, was both the most time-consuming and the poorest-performing. TITAN, though competitive with EAGLE, required markedly more compute (second slowest overall).

Medical imaging datasets often contain limited samples per class, prompting few-shot or low-resource scenarios. We first assessed linear probing on EAGLE (and other slide encoder) embeddings with $k = 1, 2, 4, 8, 16, 32$ samples per class using logistic regression. To ensure meaningful comparisons, we selected only the top three binary tasks per cancer type based on AUROC in the main results, as linear probing performs poorly on low-performance tasks, increasing randomness and diluting differences between models. While performance dips in this challenging setting, both EAGLE and TITAN consistently outperformed others. EAGLE performed best in all cancer types except lung, where Prism excelled. With $k = 1, 2, 4$, TITAN lead across all 12 tasks, followed closely by EAGLE, with both models achieving notable gaps over others (e.g., $k=4$: TITAN/EAGLE AUROC = 0.72, Prism = 0.68, Prov-GigaPath = 0.58). At $k = 8, 16, 32$, EAGLE surpassed all other models, showcasing the advantage of its focused tile selection in low-data settings (**Figure 2d, Figure S6**).

We further evaluated EAGLE and other slide-encoder vs. tile-encoder models by training regular multilayer perceptron (MLP) classifiers on 300, 150, or 75 patients. Over 29 tasks with sufficient data, EAGLE maintained the highest average AUROC across all three subsets, particularly at 150 patients (0.689 vs. 0.669 for TITAN and 0.618 for the best tile encoder) (**Figure 3e, S7**). This robust performance gap highlights how slide-level embeddings support model training when only small cohorts are available. To demonstrate EAGLE's practicality for rare-biomarker discovery, we

examined almost 300 biomarkers in a multicenter cohort of over 1,000 patients. The entire processing time from the raw images to the final predictions took <24 hours and we detected 20 biomarkers with AUROCs >0.800 (**Figure 3f, Table S2**).

Together, these efficiency metrics confirm that EAGLE's guided, two-step approach minimizes computation without compromising performance and scales well to large or multi-task pathology pipelines. EAGLE's adaptability in data-constrained contexts, indicate that the combination of slide-level embeddings, selective tile processing, and efficient feature extraction yields robust performance when training data are limited.

Versatility and Interpretability of EAGLE

EAGLE generates a single, compact embedding per whole slide or patient by focusing on a small number of highly informative tiles, improving both versatility and transparency. The selection of only 25 top tiles—those identified as most relevant by the model—makes it evident which tissue regions drive the predictions. To illustrate this interpretability advantage, we examined a subset of 50 randomly selected WSIs from the DACHS CRC cohort for MSI prediction, where 35 WSIs contained pen marks. Across all top tiles of these 35 WSIs, pen marks were present in 16% of EAGLE-selected tiles compared to 23% of tiles selected by the supervised baseline, which uses Virchow2 tile embeddings aggregated with STAMP. Notably, when considering only dominant pen marks (covering >50% of the tile), EAGLE almost completely avoided them (1 %), whereas the supervised baseline selected those tiles in 15 % of cases, even though they did not provide valuable information. Expanding the analysis to include all artifacts (e.g., tissue folds, slide edges, air bubbles, oil drops, scratches, pen marks, foreign objects, dark spots, and out-of-focus regions), EAGLE-selected tiles showed artifacts in 22% of cases, compared to 32% in the tiles selected by the supervised baseline (**Figure 4b,c**). Furthermore, a board-certified pathologist inspected top selected tiles and found that EAGLE reliably focused on the most representative tumor tissue of each case. In contrast, the supervised baseline often focused on a mixture of healthy, tumorous and artifact-rich tiles, providing puzzling and sometimes contradictory features for its prediction (**Figure S8**). This capacity to confirm which tiles are chosen could further support clinical acceptance.

We then visualized slide embeddings with Uniform Manifold Approximation and Projection (UMAP)³¹. We noted that TITAN formed well-separated clusters by cancer type, while EAGLE displayed moderate clustering and surpassed CHIEF and Prov-GigaPath Slide Encoder in capturing morphological diversity (**Figure 4a**). To further evaluate embedding structure, we compared UMAP projections of CHIEF and EAGLE across 29 TCGA cohorts, observing clearer separation with EAGLE (**Figure S9**). Moreover, we explored slide-search applications, wherein a query WSI's embedding was compared against a database of stored slide embeddings for quick retrieval of similar

cases, thereby enabling pathologists to rapidly find relevant reference slides, accelerating diagnosis or facilitating training^{32,33}. This approach was computationally lightweight, with near-instant matches. Qualitative reviews by a board-certified pathologist indicated that the slide search approach yielded highly similar cases both within a given cohort and across multiple cohorts. Interestingly, in a few instances, cases from other entities would be identified (e.g. a BRCA case while looking for a STAD case). This happened, when special subtypes were queried (e.g. a medullary carcinoma, which can occur both in the stomach as well as in the mammary gland) (**Figure 4d**). This could prove to be a very valuable tool, for example for cohort assembly for basket trials.

Together, these data indicate that EAGLE enables more transparent slide-level decision-making and simplifies downstream analyses such as multi-omic and clinical integration, and efficient retrieval of relevant comparator slides (**Figure 1d**).

Comparison with Multimodal Large Language Models (MLLMs)

Finally, we compared EAGLE with emerging MLLMs employing in-context learning low-resolution WSI thumbnails. Using $k=2$ examples per class in a few-shot classification setup, EAGLE embeddings combined with a lightweight logistic regression model surpassed GPT-4o's in-context classification for tasks including NSCLC subtyping, MSI prediction in CRC, and ER expression in BRCA. In NSCLC subtyping and ER expression prediction, GPT-4o usually defaulted to a single class (e.g., predicting adenocarcinoma in NSCLC and ER-positive in BRCA), while in all three tasks, including MSI prediction, its classification accuracy remained at chance level (0.5). To evaluate whether input resolution constrained GPT-4o's performance, we provided the model with EAGLE's top 25 most informative tiles instead of WSI thumbnails. Despite this targeted input, MLLM accuracy remained unchanged, suggesting that the bottleneck lies in the models' lack of pathology-specific feature representations rather than the resolution or relevance of the input (**Figure 2e, S10a**). Interestingly, despite its poor predictive accuracy, GPT-4o's textual responses frequently referenced key diagnostic features, such as "mucin production" and "keratinization" for NSCLC subtyping, "lymphocytic infiltration" for MSI status prediction, indicating an awareness of relevant pathological concepts (**Figure S10b**).

Taken together, these results underscore the limitations of general-purpose MLLMs in specialized pathology tasks and highlight the need for domain-adapted models. While MLLMs such as GPT-4o demonstrate impressive contextual reasoning and linguistic capabilities, their ability to generalize to specialized pathology biomarker tasks is notably limited.

Discussion

Weakly supervised CPath has fundamentally reshaped cancer research, allowing diagnosis, biomarker status prediction, and survival outcome estimation directly from WSIs. Recent progress with pathology foundation models, often trained using self-supervised learning (SSL), has enriched these pipelines, enhancing accuracy and generalizability across diverse clinical tasks. However, concerns remain about the scalability of tile-level methods and the difficulty of interpreting predictions when massive neural networks process thousands of patches per slide. Here, we introduced EAGLE, a slide-encoder framework that emulates how pathologists target limited, high-yield regions.

EAGLE's design centers on processing only 25 tiles per WSI, a strategy that substantially reduces computational requirements while preserving predictive power. This approach aligns with established clinical practice, in which pathologists focus on diagnostically relevant or suspicious tissue regions rather than exhaustively scanning each tile. Our results show that EAGLE cuts feature extraction times dramatically compared to tile-level pipelines relying on resource-intensive foundation models. These efficiency gains translate to quicker classifier training and inference, making EAGLE especially suited for large-scale or multi-institutional datasets. Such performance improvements are likely to be essential for real-time or near-real-time diagnostic workflows. Our comparative evaluations indicate that EAGLE frequently outperforms or matches leading slide- and tile-encoder baselines, particularly in biomarker prediction tasks central to precision oncology. Whereas many CPath models demonstrate high performance for commonly studied tasks such as tumor subtyping, they can struggle in more challenging settings like molecular status prediction for biomarkers or survival analyses. EAGLE addresses these obstacles by focusing on the regions that matter most morphologically, offering refined predictive performance.

A hallmark of EAGLE's design is the generation of a single, interpretable embedding per slide or patient. These embeddings perform well across various tasks—from diagnosing specific tumor subtypes to identifying molecular alterations—and open opportunities for novel applications, including content-based slide retrieval, clustering analysis, and multi-omics studies. By compressing the most relevant morphological cues into a single vector, EAGLE provides an efficient entry point for deeper integration with genomic, transcriptomic, or radiologic data. In the long term, such patient-level embeddings could serve as the backbone of comprehensive multimodal models, enabling more holistic characterizations of disease states and potentially leading to improved outcomes. Deep learning systems are often perceived as “black boxes” with limited transparency in medical settings. While the precise morphological features driving predictions within the selected 25 tiles remain elusive, and CHIEF's selection process is not fully interpretable, EAGLE offers a structured mechanism for verifying that chosen tiles are diagnostically meaningful. This capacity

to inspect and validate the most informative regions promotes trust in model predictions and ensures that decisions are not driven by artifacts such as pen markings or irrelevant features³⁴. Beyond building trust with clinicians, interpretability tools that highlight suspicious tissue patches can also streamline quality control, enabling prompt rectification of systematic errors in data or labeling. The field of CPath is expanding beyond image-only pipelines into vision language models or MLLMs that can annotate slides in a chatbot-like manner but reveal significant limitations in specialized tasks. Despite referencing key diagnostic features, GPT-4o fails to achieve accuracy beyond chance levels in biomarker prediction, even when provided with EAGLE's selected tiles. While MLLMs may complement traditional approaches in interpretability, their predictive capacity in pathology remains limited without domain adaptation.

Although we tested EAGLE extensively on multiple external cohorts spanning four major cancer types, additional large-scale validation is warranted to assess its performance on less common or rare pathologies. Furthermore, our approach might show some limitations for tasks which focus on very specific tissue areas (e.g. detection of vascular invasion) or in highly heterogeneous tumors (e.g. consisting of various subtypes). Our study prioritizes benchmarking predictive performance over detailed confounder analysis, as we focus on common predictive targets to ensure comparability across models. While this facilitates systematic evaluation, it does not capture the influence of confounding variables or the deeper morphological basis of predictions. As training datasets primarily originate from major cancer centers, they may not fully reflect the diversity of global patient populations, highlighting the need for broader validation across more heterogeneous cohorts. While EAGLE achieved AUROCs >0.900 for some tasks, the average AUROC of 0.742 indicates that EAGLE's performance might not yet be adequate to replace standard clinical procedures. Future work may explore prospective clinical trials to evaluate real-world diagnostic improvements, as well as the integration of EAGLE's embeddings with patient-specific data, such as laboratory values or electronic health records. While our results demonstrate EAGLE's resilience in limited-data scenarios, ongoing advancements in foundation model design—such as more varied SSL approaches, larger and more diverse training datasets, and refined text–image alignments—may further boost EAGLE's adaptability. Finally, the shift from tile-level to slide-level encoding techniques, although highly promising, will likely benefit from more specialized architectures tailored for niche tasks (e.g., rare tumor detection, complex survival analyses).

Author contributions

PN, TL and JNK designed the study. PN and TL developed the software. PN, MG, RL, BD, LAB, AJF, ELG, AG, SB, MJG, RS, HMB, CR, TH, UP, AIP, GC, NF, AM, MH, HB and JNK contributed to data collection and assembly. PN, TL, SF, CMLL, JC, LAS and JNK interpreted and analyzed the data. All authors substantially contributed to writing and reviewing the report, approved the final version for submission, and have agreed to be personally accountable for

the author's own contributions and to ensure that questions related to the accuracy or integrity of any part of the work, even ones in which the author was not personally involved, are appropriately investigated, resolved, and the resolution documented in the report.

Acknowledgements

The authors gratefully acknowledge the GWK support for funding this project by providing computing time through the Center for Information Services and HPC (ZIH) at TU Dresden.

Disclosures

JNK declares consulting services for Bioptimus, France; Owkin, France; DoMore Diagnostics, Norway; Panakeia, UK; AstraZeneca, UK; Scailyte, Switzerland; Mindpeak, Germany; and MultiplexDx, Slovakia. Furthermore, he holds shares in StratifAI GmbH, Germany, has received a research grant by GSK, and has received honoraria by AstraZeneca, Bayer, Daiichi Sankyo, Eisai, Janssen, MSD, BMS, Roche, Pfizer and Fresenius. SF has received honoraria from MSD and BMS. MG has received honoraria for lectures sponsored by Techniker Krankenkasse (TK) and AstraZeneca. RL declares consulting services and honoraria from MSD, Janssen, AstraZeneca, Astellas, Roche. UP declares consulting services for AbbVie and her husband is holding individual stocks for the following companies: BioNTech SE – ADR, Amazon, CureVac BV, NanoString Technologies, Google/Alphabet Inc Class C, NVIDIA Corp, Microsoft Corp. AM has received honoraria as a consultant, advisor or speaker from Roche, Lilly and Menarini/Stemline, and has received support for accommodation and travel from AstraZeneca, all outside the submitted work. NF: Consulting/advisory role: MSD, Merck, Novartis, AstraZeneca, Sysmex, Roche, Menarini Group, Gilead, Veracyte, Sakura, Abbvie. Speaker bureau: MSD, Novartis, AstraZeneca, Daiichi Sankyo, Sysmex, GSK, Gilead, Roche, Menarini, Leica Biosystems, ThermoFisher, Genomic Health, Veracyte, Lilly. Research grants: Novartis, Gilead, AstraZeneca, GSK, Pfizer. Travel grants: Roche, Novartis. No other conflicts of interest are declared by any of the authors.

Funding

JNK is supported by the German Cancer Aid (DECADE, 70115166), the German Federal Ministry of Education and Research (PEARL, 01KD2104A, 01KD2104C; CAMINO, 01EO2101; SWAG, 01KD2215A; TRANSFORM LIVER, 031L0312A; TANGERINE, 01KT2302 through ERA-NET Transcan; Come2Data, 16DKZ2044A; DEEP-HCC, 031L0315A), the German Academic Exchange Service (SECAI, 57616814), the German Federal Joint Committee (TransplantKI, 01VSF21048) the European Union's Horizon Europe and innovation programme (ODELIA, 101057091; GENIAL, 101096312), the European Research Council (ERC; NADIR, 101114631), the National Institutes of Health (EPICO, R01 CA263318) and the National Institute for Health and Care Research (NIHR, NIHR203331) Leeds Biomedical Research Centre. The views expressed are those of the author(s) and not necessarily those of the NHS, the NIHR or the Department of Health and Social Care. This work was funded by the European Union. Views and opinions expressed are however those of the author(s) only and do not necessarily reflect those of the European Union. Neither the European Union nor the granting authority can be held responsible for them. SF is supported by the German Federal Ministry of Education and Research (SWAG, 01KD2215C), the German Cancer Aid (DECADE, 70115166 and TargHet, 70115995) and the German Research Foundation (504101714). The

DACHS study was supported by the German Research Council (BR 1704/6-1, BR 1704/6-3, BR 1704/6-4, CH 117/1-1, HO 5117/2-1, HO 5117/2-2, HE 5998/2-1, HE 5998/2-2, KL 2354/3-1, KL 2354 3-2, RO 2270/8-1, RO 2270/8-2, BR 1704/17-1, BR 1704/17-2); the Interdisciplinary Research Program of the National Center for Tumor Diseases (NCT), Germany; and the German Federal Ministry of Education and Research (01KH0404, 01ER0814, 01ER0815, 01ER1505A, and 01ER1505B). JC is supported by the Mildred-Scheel-Postdoktorandenprogramm of the German Cancer Aid (grant #70115730). AM is supported by the European Society for Medical Oncology José Baselga Fellowship for Clinician Scientists founded by AstraZeneca (2023–2025). The Genetics and Epidemiology of Colorectal Cancer Consortium (GECCO) is funded by: National Cancer Institute, National Institutes of Health, U.S. Department of Health and Human Services (U01 CA137088, R01 CA488857, P20 CA252733, P50 CA285275). Genotyping/Sequencing services were provided by the Center for Inherited Disease Research (CIDR) contract number HHSN268201700006I. This research was funded in part through the NIH/NCI Cancer Center Support Grant P30 CA015704. Scientific Computing Infrastructure at Fred Hutch funded by ORIP grant S10OD028685. The CORSA study was funded by Austrian Research Funding Agency (FFG) BRIDGE (grant 829675, to Andrea Gsur), the “Herzfelder’sche Familienstiftung” (grant to Andrea Gsur) and was supported by COST Action BM1206. CRA was supported by the National Institutes of Health grant R01 CA068535. The coordination of EPIC is financially supported by the International Agency for Research on Cancer (IARC) and also by the Department of Epidemiology and Biostatistics, School of Public Health, Imperial College London which has additional infrastructure support provided by the NIHR Imperial Biomedical Research Centre (BRC). The national cohorts are supported by: Danish Cancer Society (Denmark); Ligue Contre le Cancer, Institut Gustave Roussy, Mutuelle Générale de l’Education Nationale, Institut National de la Santé et de la Recherche Médicale (INSERM) (France); German Cancer Aid, German Cancer Research Center (DKFZ), German Institute of Human Nutrition Potsdam-Rehbruecke (DIfE), Federal Ministry of Education and Research (BMBF) (Germany); Associazione Italiana per la Ricerca sul Cancro-AIRC-Italy, Compagnia di SanPaolo and National Research Council (Italy); Dutch Ministry of Public Health, Welfare and Sports (VWS), Netherlands Cancer Registry (NKR), LK Research Funds, Dutch Prevention Funds, Dutch ZON (Zorg Onderzoek Nederland), World Cancer Research Fund (WCRF), Statistics Netherlands (The Netherlands); Health Research Fund (FIS) - Instituto de Salud Carlos III (ISCIII), Regional Governments of Andalucía, Asturias, Basque Country, Murcia and Navarra, and the Catalan Institute of Oncology - ICO (Spain); Swedish Cancer Society, Swedish Research Council and and Region Skåne and Region Västerbotten (Sweden); Cancer Research UK (14136 to EPIC-Norfolk; C8221/A29017 to EPIC-Oxford), Medical Research Council (1000143 to EPIC-Norfolk; MR/M012190/1 to EPIC-Oxford) (United Kingdom). The IWHS study was supported by NIH grants CA107333 (R01 grant awarded to P.J. Limburg) and HHSN261201000032C (N01 contract awarded to the University of Iowa). The WHI program is funded by the National Heart, Lung, and Blood Institute, National Institutes of Health, U.S. Department of Health and Human Services through contracts 75N92021D00001, 75N92021D00002, 75N92021D00003, 75N92021D00004, 75N92021D00005. This work was partially supported by the Italian Ministry of Health through Ricerca Corrente 5 × 1000 funds; the Italian Ministry of Innovations via the Sustainable Growth Fund – Innovation Agreements under the Ministerial Decree of December 31, 2021, and the Director’s Decree of November 14, 2022 (2nd Call), Project No.: F/350104/01–02/X60; and the Italian Ministry of University and Research (MUR) 2023 through the “Future Artificial Intelligence Research – FAIR” program, PE0000013, CUP D53C22002380006, within the National Recovery and Resilience Plan (PNRR), Mission 4, Component 2, Investment 1.3 – funded by the European Union – NextGenerationEU. Project: “AIDH – Adaptive AI Methods for Digital Health.” We kindly thank all individuals who agreed to participate in the CORSA study. Furthermore, we thank all cooperating physicians and students and the Biobank Graz of the Medical University of Graz. We also acknowledge the TCGA Research Network and the Clinical Proteomic Tumor Analysis Consortium (CPTAC), which generated the data on which some of the results shown in this study are based. Where authors are identified as personnel of the International Agency for Research on Cancer/World Health Organization, the authors alone

are responsible for the views expressed in this article and they do not necessarily represent the decisions, policy or views of the International Agency for Research on Cancer/World Health Organization. The authors thank the WHI investigators and staff for their dedication, and the study participants for making the program possible. A full listing of WHI investigators can be found at: <https://s3-us-west-2.amazonaws.com/www-who-org/wp-content/uploads/WHI-Investigator-Long-List.pdf>

Figures

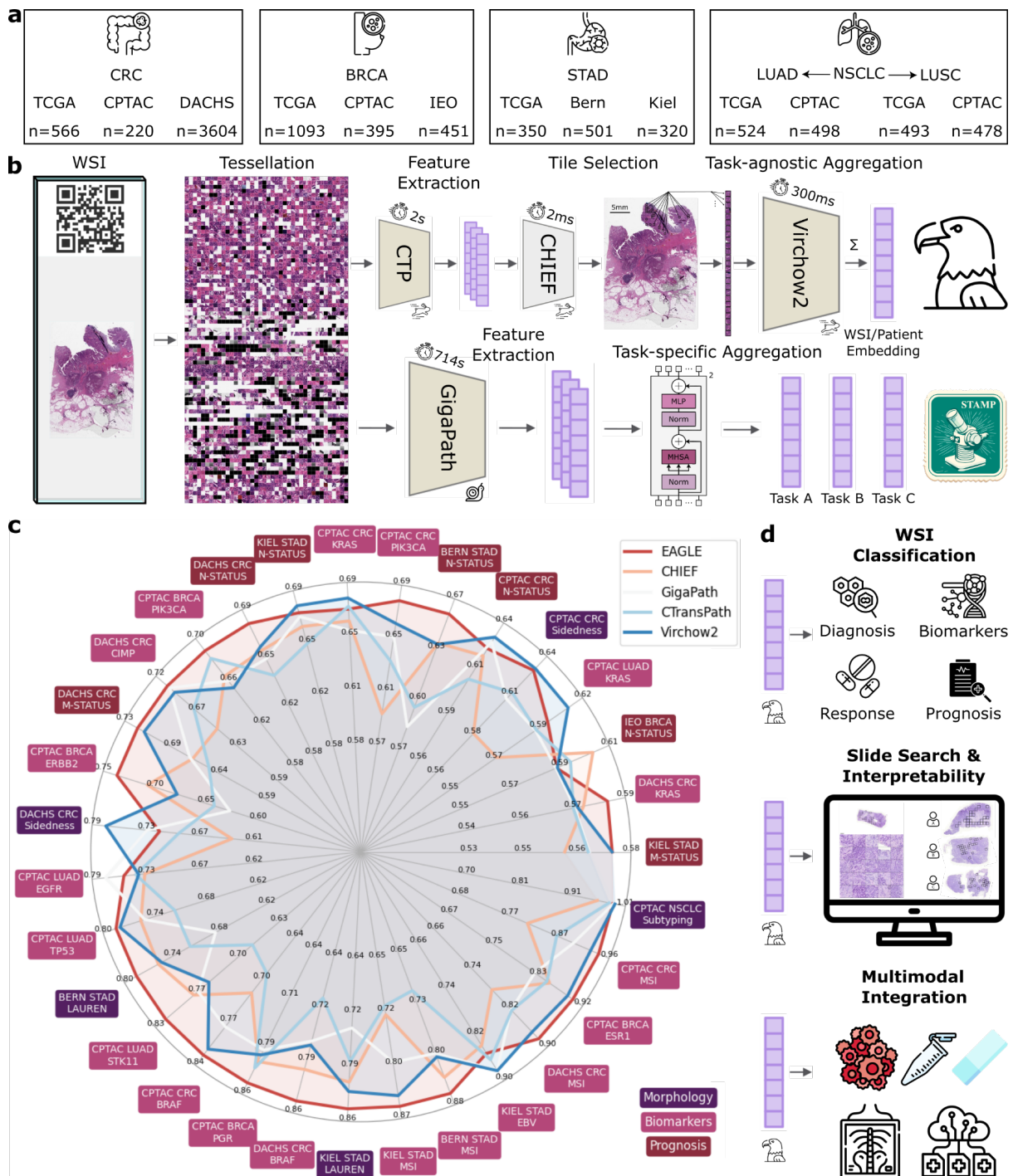


Figure 1: EAGLE framework. a) EAGLE is compared to state-of-the-art foundation models on 9,528 whole slide images (WSIs) across 13 cohorts, encompassing four cancer types. b) Workflow comparison of EAGLE and conventional supervised approaches. WSIs undergo tessellation into tiles, followed by feature extraction and aggregation. EAGLE employs a three-step process: tile feature extraction with CTransPath, tile selection using CHIEF, and detailed

feature extraction of 25 selected tiles using Virchow2, culminating in an averaged WSI embedding per patient. In contrast, supervised pipelines, such as STAMP, extract features from all tiles using models like Prov-GigaPath and aggregate these features using task-specific architectures (e.g., transformers). Measured time for average foundation model processing per WSI is included (EAGLE at 2 MPP vs. conventional supervised models at the commonly used 0.5 MPP). **c)** average AUROC scores comparing EAGLE against CHIEF, Prov-GigaPath, CTransPath, and Virchow2 across 31 computational pathology tasks. **d)** Applications of WSI/patient embeddings, including WSI classification for diagnosis, biomarker analysis, treatment response prediction, and prognosis; slide retrieval for similar-case search in clinical workflows; and integration into AI-powered clinical systems and multi-omics modeling.

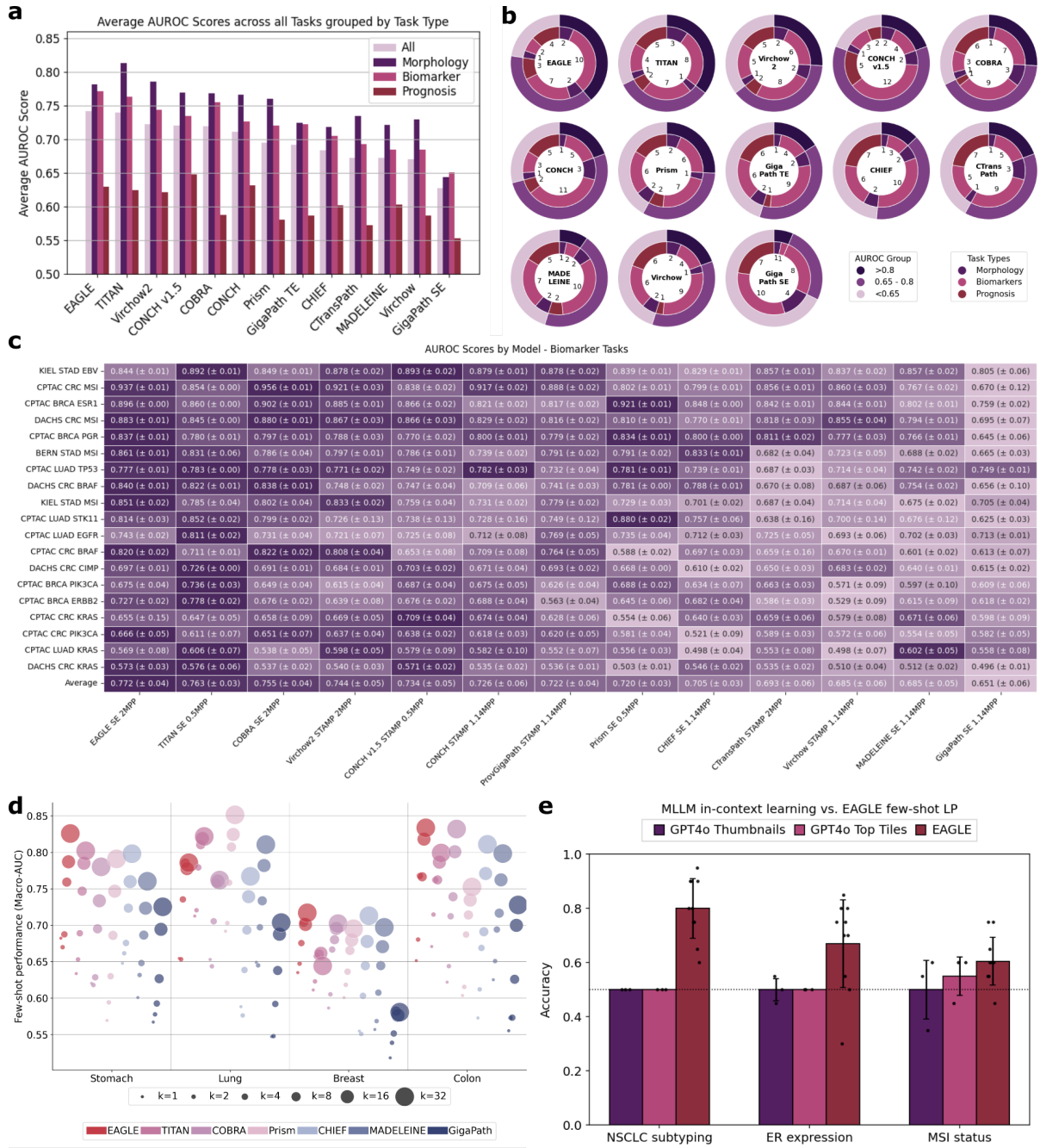


Figure 2: Comparative performance of EAGLE vs. tile- and slide-level foundation models. a) Average AUROC scores per task category across five folds for 13 models evaluated on 31 tasks. b) Distribution of tasks by model performance, showing the number of tasks where each model achieves an average AUROC of >0.800, 0.650 - 0.800, or <0.650, grouped by task type. c) Average AUROC scores for 19 biomarker prediction tasks (mean ± SD across five folds). Taskwise color normalization for better comparison of the models. Tasks are sorted by their mean AUROC across all models, while models are sorted by their mean AUROC across all tasks. d) Few-shot performance of slide encoders using linear probing with logistic regression for k=1, 2, 4, 8, 16, and 32 samples per class. To ensure robust evaluation, only

the top three binary tasks per cancer type (selected based on highest AUROC across all models) are included. **e)** Comparison of EAGLE's few-shot linear probing (using $k=2$ examples per class) versus GPT-4o's in-context learning ($k=2$) for ER expression prediction in BRCA, MSI status in CRC, and NSCLC subtyping.

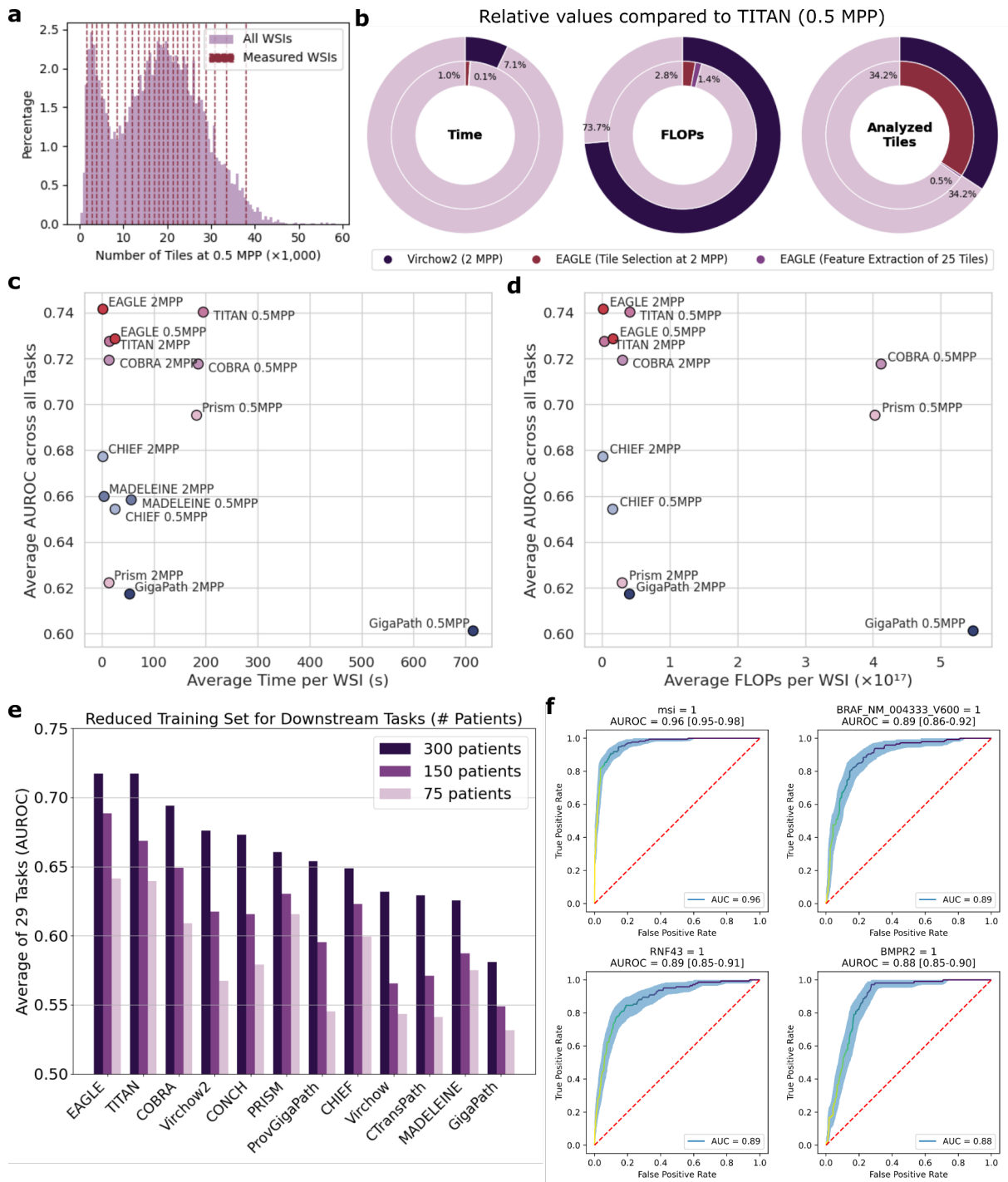


Figure 3: Computational efficiency and performance in scarce data scenarios. **a**) Tile distribution across 9,528 whole slide images (WSIs) at 0.5 MPP, with 25 WSIs sampled at regular intervals from the 2nd to the 98th percentile for timing experiments. These WSIs (mean: 17,771 tiles) differ by less than 0.3% from the dataset-wide average (17,819 tiles). **b**) Time, floating point operations (FLOPs), and number of analyzed tiles for processing 25 WSIs with EAGLE and Virchow2 at 2 MPP, normalized to TITAN at 0.5 MPP. EAGLE metrics are split into the tile selection step consisting of CTransPath and CHIEF inference and the feature extraction of selected tiles

using Virchow2. These models and magnifications were chosen as they achieve the highest average AUROC scores in their respective optimal settings. **c, d)** Time (**c**) and FLOPs (**d**) comparisons across models, plotted against AUROC performance across 31 tasks. FLOPs include tile extraction; time includes both tile and slide processing. **e)** AUROC performance of seven slide encoders and their tile-based counterparts across 29 tasks, for classifiers trained with 300, 150 or 75 patients. **f)** AUROC curves for four biomarkers with high predictive performance (MSI status, *BRAF V600*, *RNF43*, and *BMP2* mutations) from a dataset of over 1,000 patients across multiple centers. All biomarkers with an observed AUROC > 0.800 are listed in **Table S2**.

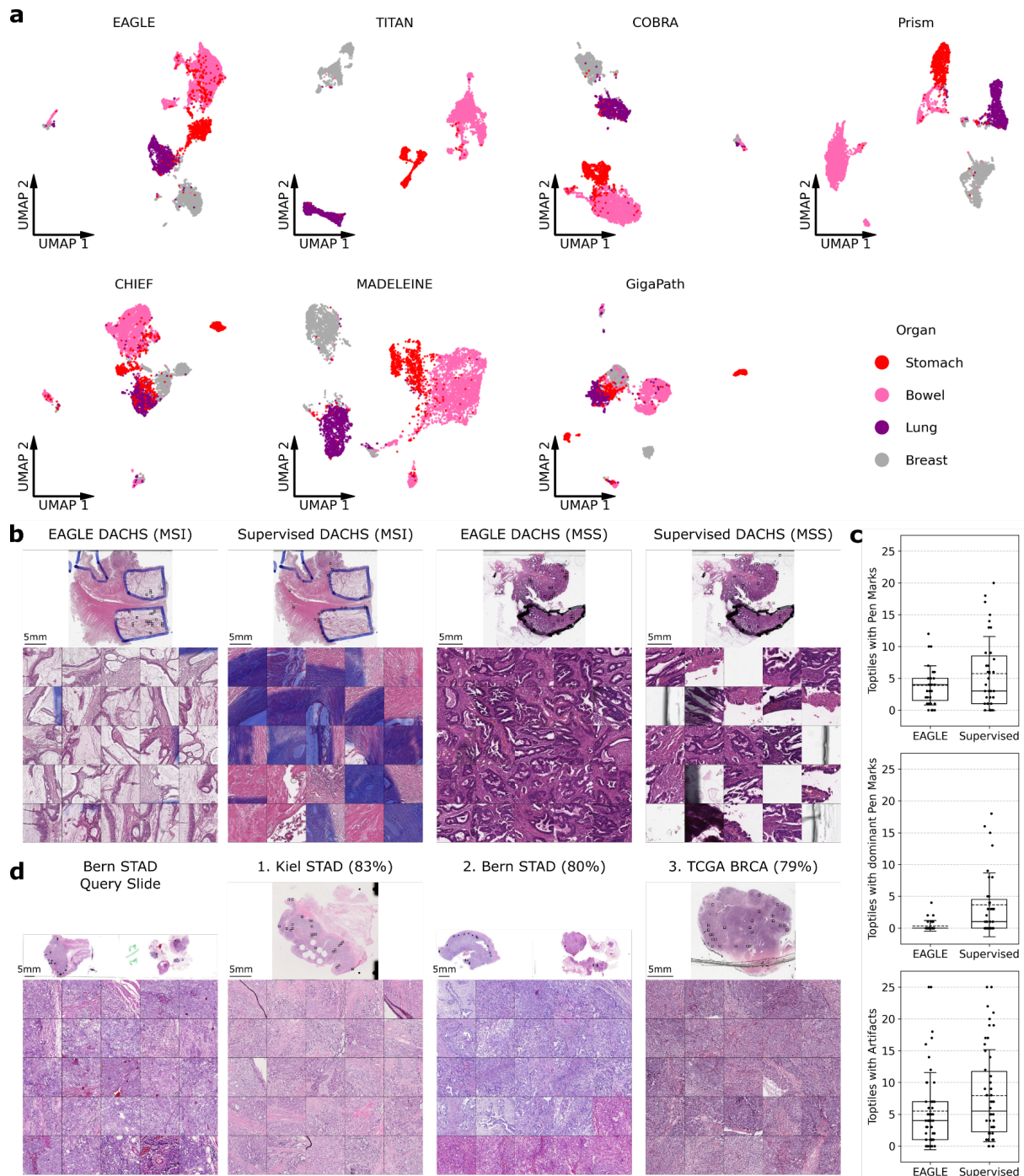


Figure 4: Versatility and interpretability. **a)** UMAPs of slide embeddings generated by EAGLE and tested slide encoders. Four tissue types are color-coded, illustrating separation by tissue type across models. **b)** Comparison of the top 25 tiles selected by EAGLE versus the supervised baseline on MSI status prediction (Virchow2 embeddings aggregated via the STAMP pipeline) for two representative DACHS slides (one MSI and one MSS case). The supervised baseline frequently highlights background, slide edge, pen mark, and other artifacts, whereas EAGLE predominantly selects representative, tissue-relevant regions. **c)** Prevalence of artifacts among top tiles from 50 randomly chosen DACHS WSIs. For each slide, the number of top tiles containing pen marks,

dominant pen marks (covering $\geq 50\%$ of the tile), or other artifacts (e.g. tissue folds, slide edges, air bubbles, oil drops, scratches, foreign objects, dark spots, and out-of-focus regions) are shown for EAGLE and the supervised baseline. The median is shown as a solid center line, and the mean with standard deviation is represented by a dashed line and error bars. **d)** Examples of slide retrieval using EAGLE's embedding space. For a given query slide, the nearest neighboring slides across all cohorts are displayed, demonstrating EAGLE's potential for similar-case search in clinical workflows. The percentages indicate the cosine similarity between the query patient embedding from the Bern cohort and the three closest patient embeddings in the feature space.

Materials and Methods

Ethics statement

This study was conducted in accordance with the Declaration of Helsinki. Both TCGA and the Clinical Proteomic Tumor Analysis Consortium (CPTAC) collections comprise retrospective, anonymized data, so no additional ethics approval was required. The DACHS study is an epidemiological study overseen by the German Cancer Research Center (DKFZ, Heidelberg, Germany) and was approved by the ethics committee of the Medical Faculty of the University of Heidelberg (reference 310/2001).

Datasets

All models used in this study, except where explicitly noted, were trained exclusively on TCGA whole-slide images (WSIs), which included histopathology data from lung adenocarcinoma (LUAD), lung squamous cell carcinoma (LUSC), colorectal cancer (CRC), stomach adenocarcinoma (STAD), and breast cancer (BRCA). External validation was carried out on CPTAC (including CPTAC-2 and CPTAC-3 prospective cohorts from 2018 and 2020, covering LUAD, LUSC, COAD, and BRCA), DACHS (CRC), proprietary STAD datasets (Kiel and Bern), and a BRCA dataset (IEO) (**Figure S11a**). None of these external cohorts were used to pretrain the foundational models or train the downstream classifiers, ensuring that no data leakage occurred. Additional information about the cohorts, including patient characteristics such as age, sex, race, cancer stage, and tumor stage, is provided in **Table S3**.

For biomarker discovery experiments (results presented in **Figures 3f**, **Table S2**), an additional dataset from the Genetics and Epidemiology of CRC Consortium (GECCO) was employed, comprising five studies: CORSA, EPIC, CRA, WHI, and IWHS^{35,36} (**Figure S11b**, **Table S4**). To ensure a minimum of 10 cases per class for both training and testing while maximizing the inclusion of biomarkers, different training and testing splits were used for each biomarker. Three centers were selected for training and two for testing, with the specific splits detailed in **Table S2** for biomarkers achieving AUROC > 0.800.

Experimental Design

Our study emulates a recently established large-scale benchmarking study²². To reflect a broad range of tasks relevant in digital pathology, three main categories were defined, namely morphological, biomarker, and prognostic tasks. Morphological tasks involved the classification of CRC slides as left or right colon (excluding transverse colon), STAD slides into Lauren subtypes, and

NSCLC slides into adenocarcinoma (LUAD) or squamous cell carcinoma (LUSC). Biomarker tasks targeted molecular or expression features such as *BRAF*, *KRAS*, *PIK3CA* mutation, microsatellite instability (MSI) and CpG island methylator phenotype (CIMP) status in CRC, EBV and MSI status in STAD, *EGFR*, *STK11*, *KRAS* and *TP53* mutation in LUAD, and HER2, ER, PR expression, and *PIK3CA* mutation in BRCA. Prognostic tasks addressed nodal involvement (N vs. N0) and metastasis (M0 vs. M+). We included only tasks with at least ten available cases per label in both training and test cohorts. In total, 31 tasks were used, and all were binary except Lauren classification (**Table S5**).

The classifiers were trained in a five-fold cross-validation setup, followed by external deployment of all folds, thereby improving statistical validity and ensuring external validation by testing exclusively on datasets not used during training. Performance metrics included AUROC, AUPRC, Balanced Accuracy, and F1 Scores and always represent the mean across the five folds.

Image Processing and Deep Learning Techniques

We adopted the STAMP v1.1.0 pipeline (see Code availability) for WSI segmentation, tile extraction, and subsequent feature generation. WSIs were divided into patches (tiles) of size 224×224 pixels (or 512×512 pixels for CONCH v1.5/TITAN, downsampled to 448×448 pixels before model inference). The final effective resolution could be 0.5, ~1.14, or 2 MPP, depending on the foundation model's magnification preference. For CONCH v1.5, due to downsampling, the effective resolutions were ~0.57 and ~2.28 MPP. Each combination of model and resolution was evaluated, with the best magnification reported in the main experiments. Tiles predominantly containing background were excluded using Canny edge detection (thresholds: 40, 100), rejecting those with fewer than 2% of pixels classified as edges³⁷. Remaining tiles were passed into a tile-level foundation model to generate feature embeddings, ranging in dimensionality from 512 (CONCH) to 1536 (Prov-GigaPath), forming an N×M matrix of tile features per WSI.

Two main approaches were taken to obtain slide-level representations. In the supervised approach, tile embeddings were fed into a task-specific aggregator, typically a transformer-based network (STAMP) or attention-based multiple instance learning (ABMIL), in order to produce supervised predictions for each classification endpoint^{18,21}. In this scenario, every new task required retraining the aggregator model. Recently, slide encoders were introduced, which combine tile embeddings (and sometimes tile coordinates) into a single embedding vector for each slide or patient. This strategy is agnostic to the specific task and thus enables a unified, unsupervised representation that can be readily extended to multiple downstream applications by training a small classifier. Detailed hyperparameters for all classifiers are listed in **Table S6**.

Our proposed EAGLE framework integrates CHIEF, a slide-level foundation model, with Virchow2, a tile-level foundation model, to efficiently generate precise WSI embeddings. EAGLE emulates the pathologist's workflow by first obtaining an overview of the entire slide, then focusing on the most relevant regions. Since EAGLE requires CTransPath tile embeddings as input, we first extracted features using CTransPath at 2 MPP. CHIEF then uses these embeddings to produce a slide-level representation and an attention vector, originally designed to aggregate tile embeddings into a single slide embedding. EAGLE repurposes this attention vector to identify the top 25 most informative tiles, mimicking how pathologists zoom in on pertinent areas. These tiles are reprocessed with Virchow2 to extract detailed feature embeddings. The resulting 25 embeddings are averaged to create a compact, unsupervised slide-level representation. This hybrid approach minimizes computational costs by applying a more powerful feature extractor only to the most informative tiles, preserving critical morphological details while avoiding unnecessary processing of less relevant regions. The final embeddings enable the use of lightweight models, such as a small MLP classifier, for downstream tasks. This efficient pipeline demonstrates a balance of performance and computational feasibility for large-scale pathology analyses.

Multiple other slide encoders and their tile-level foundations were also assessed (**Table S7,S8**). Prov-GigaPath, used a masked autoencoder scheme on 171,189 WSIs from Providence, adopting a LongNet architecture with dilated attention at the slide level and a ViT-G/14 tile encoder trained with DINOv2^{9,38}. PRISM applied a Perceiver-based architecture with CoCa-style vision-language alignment, trained on 587,196 WSIs in 195,344 specimen-report pairs, and employed a ViT-H/14 tile encoder called Virchow, which was also pretrained with DINOv2^{10,26}. CHIEF was trained via slide-level contrastive learning and anatomic site information, using CTransPath with a SwinTransformer architecture as the tile encoder^{8,23}. MADELEINE was pretrained on multistain data from breast samples using a dual global/local cross-stain alignment, and it built on CONCH, a vision-language CoCa model with 1.1 million image-text pairs^{27,29}. TITAN used a multi-stage pretraining regime combining visual self-supervision, alignment with pathology reports, and 423,122 synthetic captions generated by a multimodal AI copilot; it employed CONCH v1.5 for tile embeddings, relying on UNI as its vision backbone and CoCa's text tower^{7,28,39}. COBRA was trained on 3,048 WSIs to align tile embeddings from multiple foundation models via a contrastive loss, yielding a slide-level representation³⁰. The best version of COBRA uses Virchow2 features, which expands on Virchow by scaling its dataset to 3.1 million WSIs and using domain-specific modifications of the DINOv2 framework²⁴. COBRA and CHIEF were (partly) trained on TCGA, but none of the models used our external testing cohorts, preventing data leakage. We compared each slide encoder against a straightforward mean-pooling baseline, where tile embeddings are simply averaged to yield an unsupervised slide-level feature vector.

For certain patients with multiple WSIs (e.g., multiple tissue blocks), each slide encoder was applied in two possible ways. Either each slide was independently processed, and the embeddings

were averaged to yield a single patient representation, or all tiles were passed simultaneously into the slide encoder to produce one patient embedding per forward pass. Combining all tiles lead to higher performance of all slide encoders, but due to memory constraints on a 48 GB GPU we had to cap the maximum number of features for TITAN at 15,000.

Once a slide-level or patient-level embedding was computed, it was fed into a small multilayer perceptron (MLP) to yield final predictions for each classification task. This MLP used an input size of 768, had a hidden size of 256 with SiLU activation and dropout, and was trained for 32 epochs using a one-cycle policy with the AdamW optimizer (learning rate= 1×10^{-4} , weight decay= 1×10^{-2}). Cross-entropy loss with class weighting addressed label imbalance. Early stopping, monitored through validation loss in a five-fold cross-validation scheme, selected the best checkpoints. For few-shot linear probing experiments, we replaced the MLP with a logistic regression model (lbfgs solver, L2 penalty=1.0, 10,000 maximum iterations, and balanced class weights) and trained on $k=1, 2, 4, 8, 16, 32$ samples per class (**Figure S12, Table S6**). We repeated each setting ten times with different random draws to stabilize the results. This approach allowed us to evaluate how effectively slide encoders adapted to extremely limited training data.

To compare EAGLE with a multimodal large language model, we tested EAGLE's few-shot performance ($k=2$) against GPT-4o in-context learning on three specific tasks: NSCLC subtyping (LUAD vs. LUSC), MSI status prediction in CRC, and ER expression in BRCA. EAGLE used its standard logistic regression approach, while GPT-4o received prompts containing two example images per class, plus the query image (top 25 EAGLE-selected tiles vs. a single thumbnail) (**Table S9**). The GPT-4o model was run three times per image to reduce variability, with temperature=0.7 and a maximum token length of 1,000. A strict JSON format in the prompt forced GPT-4o to provide a single label in each response.

An additional analysis was conducted to examine computational efficiency. We selected 25 representative WSIs (at percentiles 2, 6, 10, ..., 98 by tile count) and measured the inference time and floating-point operations (FLOPs) for each tile encoder. FLOP counts were derived using ptflops and were multiplied by the average tile count in the overall dataset to estimate total computational costs.

Interpretability

To interpret the embedding spaces generated by EAGLE, we applied UMAP dimensionality reduction ($n_neighbors=15$, $min_dist=0.1$) to project patient embeddings from all cohorts into two dimensions. This visualization enabled the assessment of morphological clustering by tissue origin. Separate experiments tested how EAGLE's embeddings facilitated slide-level retrieval by normalizing

each embedding with L2 and performing a cosine similarity search. We queried five random patients per external cohort and returned the top three matches. The retrieved slides were assessed by a board-certified pathologist regarding the quality and importance of the selected regions of the WSIs.

Furthermore, to investigate the robustness of EAGLE's top-tile selection, particularly in the presence of artifacts, we conducted a systematic review of its top 25 tiles on 50 randomly selected slides from the DACHS CRC cohort. A board-certified pathologist reviewed these tiles to determine the frequency of artifact focus (e.g., pen marks) versus tumor-rich regions. This performance was compared to a supervised baseline: Virchow2 tile embeddings were aggregated in STAMP on the MSI status prediction task. The 25 tiles receiving the highest attention weights were identified using Gradient-weighted Class Activation Mapping (Grad-CAM)⁴⁰. A board-certified pathologist analyzed the tiles selected by both EAGLE and STAMP, focusing on their clinical relevance and morphological significance.

Statistical Analysis

All classification performance results across tasks were aggregated from the five models produced in each cross-validation fold and summarized via metrics such as mean AUROC, AUPRC, balanced accuracy, and F1. Standard deviations were computed across the five folds, and two-sided DeLong's tests were applied to ensembled predictions (averaging fold probability scores for each sample) to assess differences in AUROC. Multi-class tasks like Lauren classification were excluded from these statistical tests because DeLong's procedure is not directly applicable in the multi-class setting. Throughout, we used Benjamini–Hochberg adjustments and considered p-values below 0.05 as evidence of statistical superiority.

Data availability

WSIs from TCGA are publicly accessible through the Genomic Data Commons Data Portal (<https://portal.gdc.cancer.gov/>), and CPTAC slides can be obtained from the CPTAC Data Portal (<https://proteomics.cancer.gov/data-portal>). All molecular data for these resources is available in cBioPortal (<https://www.cbioportal.org/>). The slides and biomarker data for DACHS were generated for prior studies^{41–43} with restricted access. Biomarker data for DACHS are available by requesting Authorized Access to the phs001078 study [https://www.ncbi.nlm.nih.gov/projects/gap/cgi-bin/study.cgi?study_id=phs001113.v1.p1]. Applications for access to DACHS biomarker data are reserved for Senior Investigators and NIH Investigators as defined in <https://dbgap.ncbi.nlm.nih.gov/aa/wga.cgi>, and upon successful application grants access to the data for 1 year with the option to renew access. The slides for DACHS can only be requested directly through the DACHS principal investigators. All other cohorts can be requested

from the respective study investigators. The data generated in this study for the creation of the figures are provided in the Source Data file. Source data are provided with this paper.

Code availability

All benchmarking experiments build upon open-source STAMP software (v1.1.0). Publicly available foundation models (e.g., CTransPath, Prov-GigaPath, CONCH, Virchow, Virchow2, etc.) are accessible via GitHub (<https://github.com/KatherLab/STAMP-Benchmark>) under permissive licenses. The implementation of EAGLE, tested slide encoders, implementations of the MLP and LP classifiers, the GPT-4o-based in-context learning, UMAP visualization, top tiles and slide search are provided within the EAGLE repository (<https://github.com/KatherLab/EAGLE>). All experiments were conducted using NVIDIA RTX A6000, L40 or H100 GPUs.

References

1. Coudray, N. *et al.* Classification and mutation prediction from non-small cell lung cancer histopathology images using deep learning. *Nat. Med.* **24**, 1559–1567 (2018).
2. Kather, J. N. *et al.* Deep learning can predict microsatellite instability directly from histology in gastrointestinal cancer. *Nat. Med.* **25**, 1054–1056 (2019).
3. Lu, M. Y. *et al.* Data-efficient and weakly supervised computational pathology on whole-slide images. *Nat Biomed Eng* **5**, 555–570 (2021).
4. Campanella, G. *et al.* Clinical-grade computational pathology using weakly supervised deep learning on whole slide images. *Nat. Med.* **25**, 1301–1309 (2019).
5. Lipkova, J. *et al.* Artificial intelligence for multimodal data integration in oncology. *Cancer Cell* **40**, 1095–1110 (2022).
6. Song, A. H. *et al.* Artificial intelligence for digital and computational pathology. *Nat Rev Bioeng* **1**, 930–949 (2023).
7. Chen, R. J. *et al.* Towards a general-purpose foundation model for computational pathology. *Nat. Med.* **30**, 850–862 (2024).
8. Wang, X. *et al.* Transformer-based unsupervised contrastive learning for histopathological image classification. *Med. Image Anal.* **81**, 102559 (2022).
9. Xu, H. *et al.* A whole-slide foundation model for digital pathology from real-world data. *Nature* **630**, 181–188 (2024).
10. Vorontsov, E., Bozkurt, A., Casson, A. & Shaikovski, G. A foundation model for clinical-grade computational pathology and rare cancers detection. *Nat. Med.* (2024).
11. Lipkova, J. & Kather, J. N. The age of foundation models. *Nat. Rev. Clin. Oncol.* **21**, 769–770 (2024).
12. Lu, M. Y. *et al.* A multimodal generative AI copilot for human pathology. *Nature* **634**, 466–473 (2024).
13. Derraz, B. *et al.* New regulatory thinking is needed for AI-based personalised drug and cell therapies in precision oncology. *NPJ Precis. Oncol.* **8**, 23 (2024).

14. Tran, M. *et al.* Generating clinical-grade pathology reports from gigapixel whole slide images with HistoGPT. *medRxiv* (2024) doi:10.1101/2024.03.15.24304211.
15. Ferber, D. *et al.* In-context learning enables multimodal large language models to classify cancer pathology images. *Nat. Commun.* **15**, 10104 (2024).
16. Clusmann, J. *et al.* The future landscape of large language models in medicine. *Commun. Med.* **3**, 141 (2023).
17. Chen, R. J. *et al.* Scaling vision Transformers to gigapixel images via hierarchical self-supervised learning. *Proc. IEEE Comput. Soc. Conf. Comput. Vis. Pattern Recognit.* 16123–16134 (2022).
18. El Nahhas, O. S. M. *et al.* From whole-slide image to biomarker prediction: end-to-end weakly supervised deep learning in computational pathology. *Nat. Protoc.* (2024) doi:10.1038/s41596-024-01047-2.
19. Frascarelli, C. *et al.* Deep learning algorithm on H&E whole slide images to characterize TP53 alterations frequency and spatial distribution in breast cancer. *Comput. Struct. Biotechnol. J.* **23**, 4252–4259 (2024).
20. Shmatko, A., Ghaffari Laleh, N., Gerstung, M. & Kather, J. N. Artificial intelligence in histopathology: enhancing cancer research and clinical oncology. *Nat. Cancer* **3**, 1026–1038 (2022).
21. Ilse, M., Tomczak, J. M. & Welling, M. Attention-based deep multiple instance learning. *arXiv [cs.LG]* (2018).
22. Neidlinger, P. *et al.* Benchmarking foundation models as feature extractors for weakly-supervised computational pathology. *arXiv [eess.IV]* (2024) doi:10.48550/ARXIV.2408.15823.
23. Wang, X. *et al.* A pathology foundation model for cancer diagnosis and prognosis prediction. *Nature* **634**, 970–978 (2024).
24. Zimmermann, E. *et al.* Virchow2: Scaling self-supervised mixed magnification models in pathology. *arXiv [cs.CV]* (2024).

25. Kather, J. N. *et al.* Pan-cancer image-based detection of clinically actionable genetic alterations. *Nat Cancer* **1**, 789–799 (2020).
26. Shaikovski, G. *et al.* PRISM: A multi-modal generative foundation model for slide-level histopathology. *arXiv [eess.IV]* (2024).
27. Jaume, G. *et al.* Multistain pretraining for slide representation learning in pathology. *arXiv [eess.IV]* (2024).
28. Ding, T. *et al.* Multimodal Whole Slide Foundation Model for Pathology. Preprint at <https://doi.org/10.48550/ARXIV.2411.19666> (2024).
29. Lu, M. Y. *et al.* A visual-language foundation model for computational pathology. *Nat. Med.* **30**, 863–874 (2024).
30. Lenz, T. *et al.* Unsupervised foundation model-agnostic slide-level representation learning. *arXiv [cs.CV]* (2024).
31. McInnes, L., Healy, J. & Melville, J. UMAP: Uniform Manifold Approximation and Projection for Dimension Reduction. *arXiv [stat.ML]* (2018) doi:10.48550/ARXIV.1802.03426.
32. Shang, H. H. *et al.* Histopathology slide indexing and search — are we there yet? *NEJM AI* **1**, (2024).
33. Wang, X. *et al.* RetCCL: Clustering-guided contrastive learning for whole-slide image retrieval. *Med. Image Anal.* **83**, 102645 (2023).
34. Clusmann, J. *et al.* A pen mark is all you need - Incidental prompt injection attacks on Vision Language Models in real-life histopathology. *medRxiv* 2024.12.11.24318840 (2024) doi:10.1101/2024.12.11.24318840.
35. dbGaP Study. https://www.ncbi.nlm.nih.gov/projects/gap/cgi-bin/study.cgi?study_id=phs001078.v1.p1.
36. Gustav, M. *et al.* Assessing genotype-phenotype correlations with deep Learning in colorectal cancer: A multi-centric study. *medRxiv* (2025) doi:10.1101/2025.02.04.25321660.
37. Canny, J. A computational approach to edge detection. *IEEE Trans. Pattern Anal. Mach. Intell.* **8**, 679–698 (1986).

38. Oquab, M. *et al.* DINOv2: Learning Robust Visual Features without Supervision. *arXiv [cs.CV]* (2023).
39. Yu, J. *et al.* CoCa: Contrastive Captioners are Image-Text Foundation Models. *arXiv [cs.CV]* (2022).
40. Selvaraju, R. R. *et al.* Grad-CAM: Visual Explanations from Deep Networks via Gradient-Based Localization. *Int. J. Comput. Vis.* **128**, 336–359 (2020).
41. Lilla, C. *et al.* Effect of NAT1 and NAT2 genetic polymorphisms on colorectal cancer risk associated with exposure to tobacco smoke and meat consumption. *Cancer Epidemiol. Biomarkers Prev.* **15**, 99–107 (2006).
42. Brenner, H., Chang-Claude, J., Seiler, C. M. & Hoffmeister, M. Long-term risk of colorectal cancer after negative colonoscopy. *J. Clin. Oncol.* **29**, 3761–3767 (2011).
43. Hoffmeister, M. *et al.* Statin use and survival after colorectal cancer: the importance of comprehensive confounder adjustment. *J. Natl. Cancer Inst.* **107**, djv045 (2015).

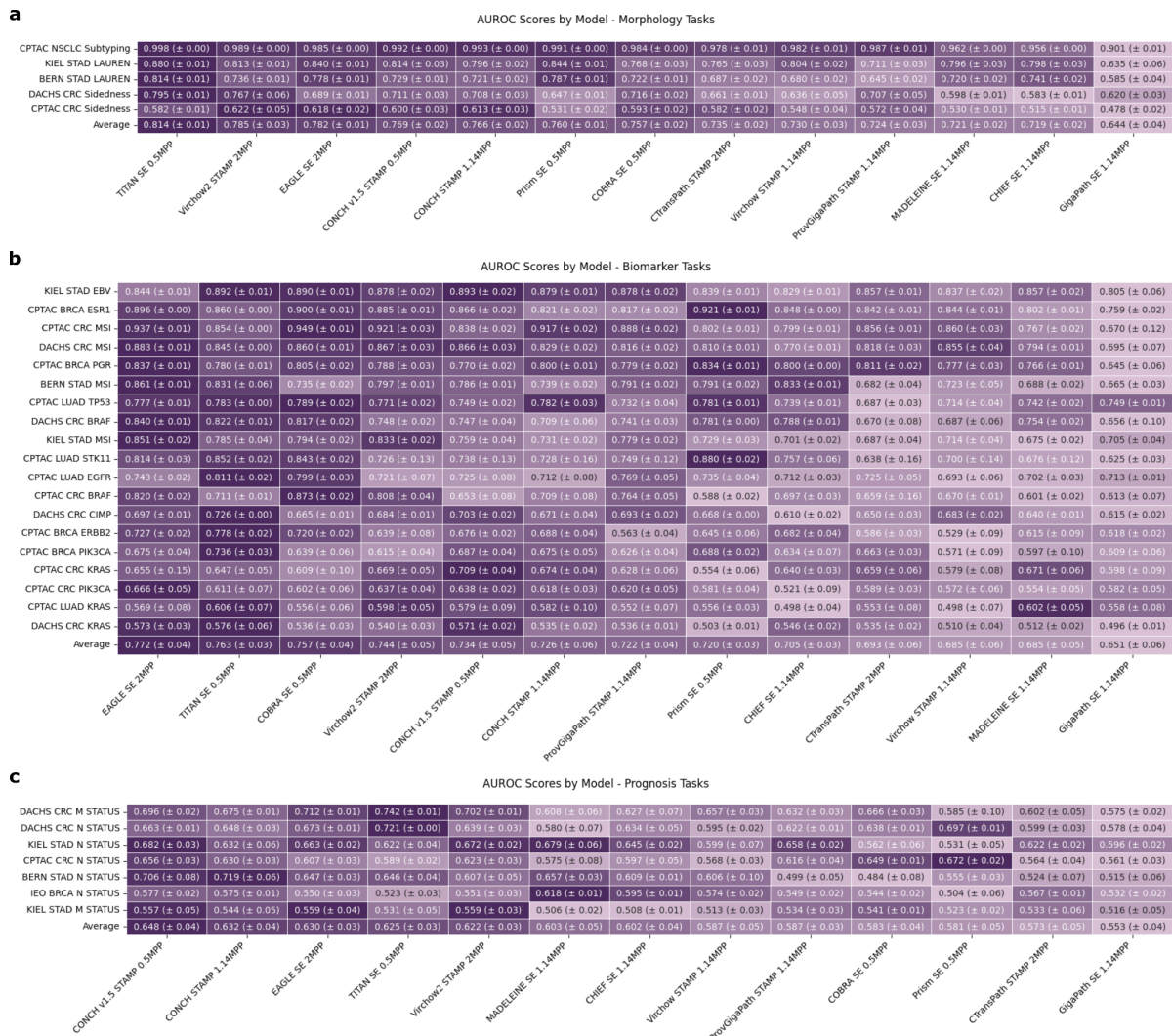
Supplementary Figures

Fig. S1: Comparison of multiple performance metrics across all models



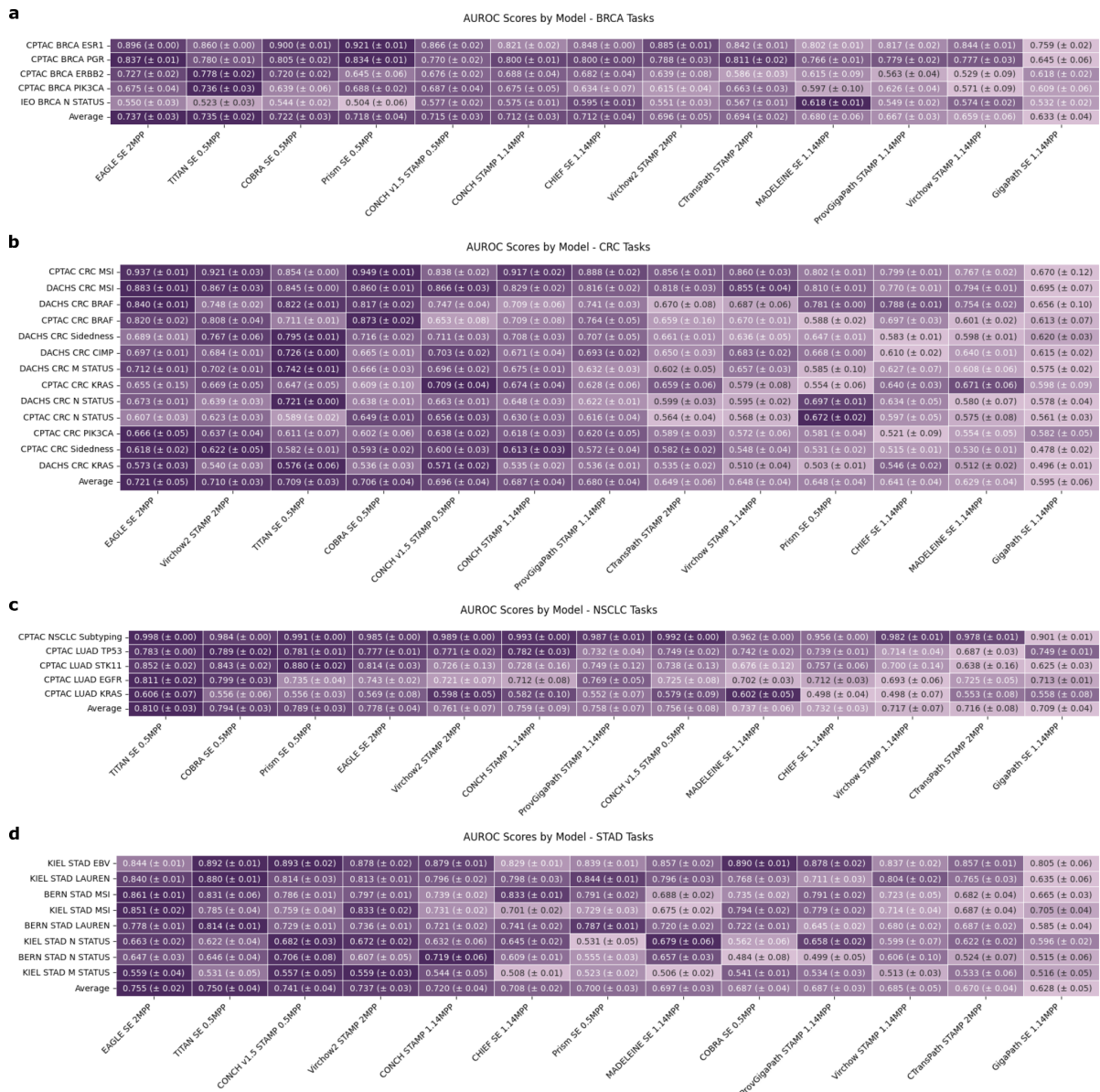
AUROC (**a**), AUPRC (**b**), balanced accuracy (**c**), and F1 (**d**) scores for the best version of each of the 13 models evaluated on 31 tasks (mean across five folds). Colormaps are normalized per task. Tasks are ordered by mean AUROC across all models and models by mean AUROC across tasks. For AUPRC and F1, the positive class is defined per task (**Table S5**); for the three-class Lauren classification, one-vs-rest metrics are macro-averaged.

Fig. S2: Task specific performance of all foundation models



Average AUROC scores (mean ± SD across five folds) for the best-performing magnification and aggregation (always STAMP) of seven slide encoders and six tile-level foundation models on (a) Morphology, (b) Biomarker, and (c) Prognosis tasks. The colormaps are normalized per task for enhanced comparison; tasks are ordered by mean AUROC across all models and models by mean AUROC across tasks.

Fig. S3: Cancer-type specific performance of all foundation models



Average AUROC scores (mean ± SD across five folds) for all 13 evaluated models stratified by cancer type: (a) BRCA, (b) CRC, (c) NSCLC, and (d) STAD. Colormaps are task-normalized, tasks are ordered by mean AUROC across all models and models by mean AUROC across tasks.

Fig. S4: Statistical significance analysis using DeLong's test

a

AUROC (5-fold Ensemble) per Task and Model

CPTAC NSCLC Subtyping	0.987	0.998	0.994	0.988	0.987	0.991	0.988	0.991	0.990	0.956	0.962	0.904
CRC CPTAC MSI	0.943	0.856	0.930	0.949	0.963	0.909	0.917	0.805	0.890	0.804	0.764	0.784
STAD Kiel EBV	0.850	0.897	0.888	0.891	0.853	0.921	0.868	0.844	0.842	0.829	0.873	0.855
BRCA CPTAC ESR1	0.899	0.861	0.827	0.912	0.907	0.831	0.857	0.927	0.856	0.848	0.805	0.780
CRC DACHS MSI	0.890	0.846	0.844	0.883	0.892	0.836	0.859	0.813	0.889	0.773	0.804	0.767
LUAD CPTAC STK11	0.827	0.860	0.865	0.872	0.817	0.831	0.794	0.895	0.864	0.789	0.770	0.633
BRCA CPTAC PGR	0.841	0.784	0.817	0.823	0.803	0.801	0.807	0.842	0.786	0.802	0.765	0.704
STAD Bern MSI	0.867	0.871	0.749	0.802	0.798	0.804	0.740	0.803	0.745	0.840	0.695	0.702
CRC DACHS BRAF	0.853	0.825	0.766	0.753	0.851	0.768	0.713	0.785	0.751	0.794	0.766	0.734
LUAD CPTAC TP53	0.795	0.790	0.814	0.783	0.787	0.758	0.740	0.788	0.733	0.749	0.744	0.759
LUAD CPTAC EGFR	0.757	0.812	0.786	0.750	0.741	0.811	0.796	0.759	0.751	0.722	0.725	0.728
STAD Kiel MSI	0.859	0.809	0.739	0.825	0.812	0.786	0.711	0.737	0.717	0.700	0.681	0.718
CRC CPTAC BRAF	0.828	0.714	0.754	0.766	0.829	0.793	0.734	0.593	0.687	0.698	0.603	0.652
CRC DACHS LEFT RIGHT	0.694	0.798	0.726	0.755	0.743	0.754	0.676	0.649	0.680	0.587	0.598	0.631
CRC DACHS M STATUS	0.719	0.745	0.699	0.716	0.719	0.673	0.670	0.674	0.686	0.683	0.666	0.591
CRC CPTAC KRAS	0.747	0.703	0.713	0.711	0.743	0.680	0.681	0.617	0.578	0.660	0.720	0.668
BRCA CPTAC PIK3CA	0.706	0.756	0.717	0.625	0.670	0.663	0.687	0.703	0.620	0.690	0.646	0.635
CRC DACHS CIMP	0.700	0.727	0.691	0.702	0.694	0.704	0.638	0.671	0.698	0.610	0.644	0.622
BRCA CPTAC ERBB2	0.720	0.786	0.708	0.707	0.679	0.558	0.617	0.660	0.555	0.706	0.660	0.635
CRC DACHS N STATUS	0.685	0.725	0.677	0.657	0.629	0.636	0.632	0.706	0.614	0.668	0.646	0.602
STAD Kiel N STATUS	0.671	0.641	0.661	0.636	0.605	0.688	0.653	0.552	0.625	0.644	0.716	0.605
CRC CPTAC PIK3CA	0.703	0.653	0.636	0.658	0.719	0.661	0.595	0.596	0.604	0.551	0.606	0.599
CRC CPTAC N STATUS	0.607	0.588	0.652	0.639	0.622	0.642	0.593	0.675	0.568	0.629	0.643	0.608
STAD Bern N STATUS	0.651	0.664	0.756	0.619	0.529	0.508	0.592	0.574	0.646	0.609	0.690	0.491
LUAD CPTAC KRAS	0.594	0.634	0.637	0.533	0.538	0.601	0.598	0.565	0.498	0.489	0.620	0.537
CRC CPTAC LEFT RIGHT	0.629	0.588	0.612	0.574	0.612	0.598	0.587	0.526	0.572	0.517	0.530	0.474
BRCA IEO N STATUS	0.552	0.518	0.590	0.559	0.577	0.561	0.571	0.473	0.582	0.595	0.623	0.543
CRC DACHS KRAS	0.597	0.612	0.548	0.576	0.553	0.542	0.542	0.518	0.538	0.544	0.513	0.491
STAD Kiel M STATUS	0.568	0.526	0.548	0.553	0.511	0.540	0.513	0.525	0.520	0.504	0.504	0.514
Average	0.750	0.744	0.736	0.732	0.730	0.719	0.702	0.699	0.693	0.689	0.689	0.654

b

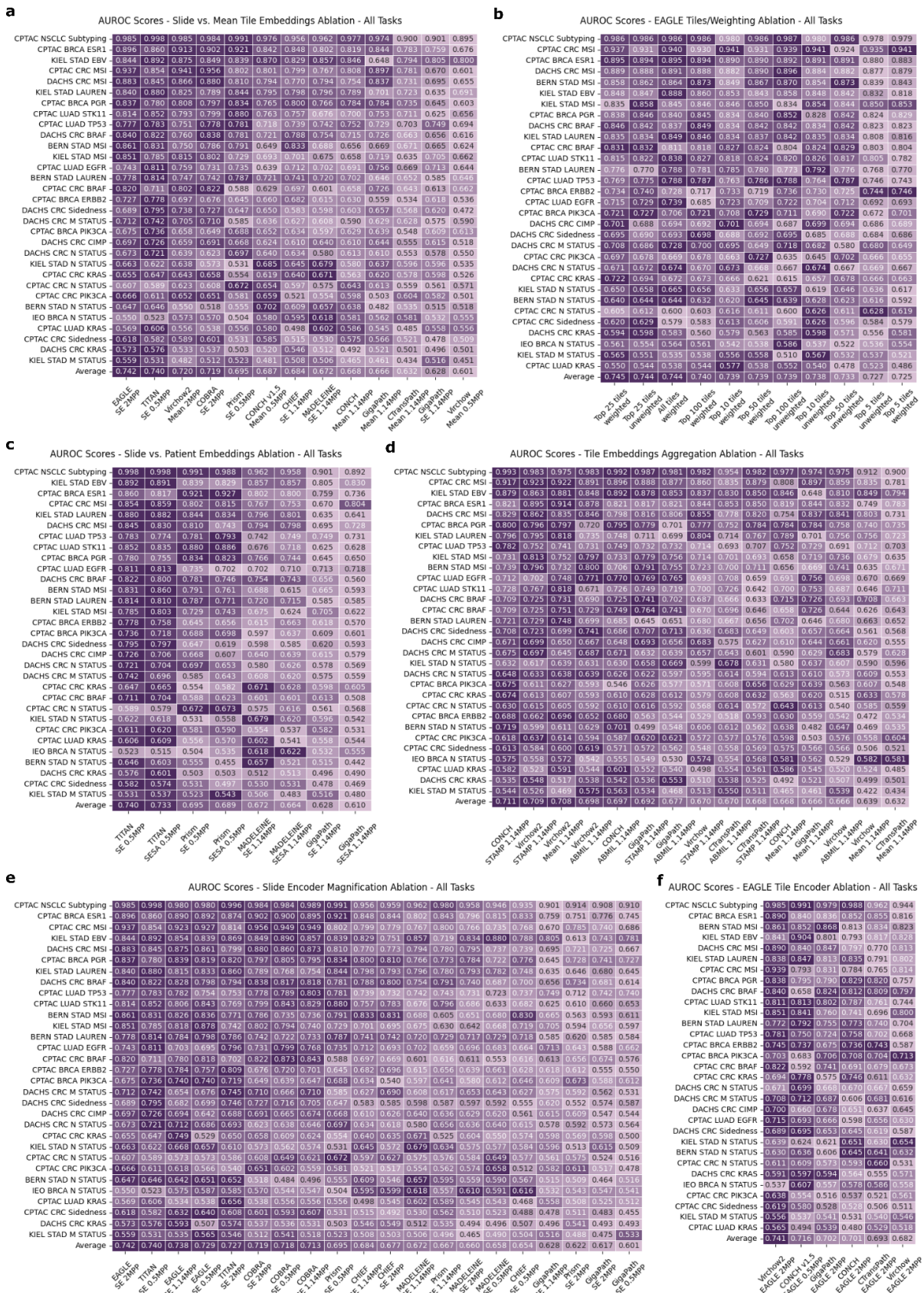
Adjusted P-Values (Benjamini-Hochberg) DeLong's Test: EAGLE vs. Other Models

CPTAC NSCLC Subtyping	0.053	0.142	0.719	0.962	0.457	0.872	0.522	0.598	0.010	0.035	2e-05
CRC CPTAC MSI	0.019	0.707	0.889	0.415	0.371	0.336	0.029	0.169	0.019	0.014	0.011
STAD Kiel EBV	0.371	0.641	0.372	0.938	0.071	0.751	0.894	0.904	0.478	0.770	0.957
BRCA CPTAC ESR1	0.301	0.005	0.561	0.739	0.041	0.154	0.371	0.301	0.045	0.003	0.011
CRC DACHS MSI	2e-05	0.006	0.678	0.838	4e-04	0.072	3e-11	0.962	3e-16	4e-07	5e-09
LUAD CPTAC STK11	0.579	0.592	0.462	0.893	0.957	0.758	0.283	0.621	0.563	0.478	0.062
BRCA CPTAC PGR	0.127	0.411	0.493	0.150	0.375	0.250	0.973	0.204	0.149	0.043	0.005
STAD Bern MSI	0.928	0.014	0.127	0.094	0.179	0.016	0.096	0.024	0.424	2e-04	9e-04
CRC DACHS BRAF	0.016	4e-07	1e-08	0.866	4e-07	4e-13	3e-04	3e-08	8e-04	2e-05	4e-07
LUAD CPTAC TP53	0.901	0.678	0.746	0.835	0.424	0.231	0.893	0.185	0.386	0.367	0.508
LUAD CPTAC EGFR	0.120	0.585	0.893	0.717	0.232	0.542	0.957	0.910	0.355	0.567	0.598
STAD Kiel N STATUS	0.185	0.001	0.347	0.346	0.035	0.001	0.026	0.010	2e-05	8e-07	0.006
CRC CPTAC BRAF	0.034	0.204	0.166	0.973	0.435	0.245	0.001	0.024	0.100	0.011	0.008
CRC DACHS LEFT RIGHT	5e-27	0.021	9e-08	3e-08	2e-06	0.318	3e-04	0.418	5e-17	5e-11	2e-05
CRC DACHS M STATUS	0.101	0.371	0.913	0.973	0.026	0.008	0.029	0.125	0.011	0.006	9e-10
CRC CPTAC KRAS	0.597	0.721	0.585	0.957	0.405	0.435	0.163	0.020	0.205	0.739	0.301
BRCA CPTAC PIK3CA	0.425	0.872	0.172	0.457	0.462	0.699	0.962	0.154	0.699	0.185	0.300
CRC DACHS CIMP	0.046	0.597	0.904	0.666	0.820	3e-06	0.031	0.938	3e-13	7e-04	1e-05
BRCA CPTAC ERBB2	0.478	0.904	0.901	0.457	0.043	0.114	0.558	0.031	0.869	0.676	0.415
CRC DACHS N STATUS	2e-04	0.606	0.046	5e-06	2e-04	1e-04	0.127	5e-07	0.123	0.013	1e-08
STAD Kiel N STATUS	0.402	0.801	0.300	0.094	0.680	0.680	0.001	0.268	0.185	0.171	0.231
CRC CPTAC PIK3CA	0.652	0.411	0.514	0.846	0.666	0.190	0.411	0.145	0.154	0.391	0.265
CRC CPTAC N STATUS	0.838	0.468	0.654	0.780	0.680	0.872	0.411	0.663	0.746	0.740	0.987
STAD Bern N STATUS	0.739	2e-04	0.300	8e-05	1e-05	0.080	0.031	0.898	0.060	0.402	4e-05
LUAD CPTAC KRAS	0.501	0.582	0.415	0.204	0.948	0.957	0.654	0.166	0.036	0.746	0.435
CRC CPTAC LEFT RIGHT	0.435	0.846	0.301	0.746	0.665	0.564	0.091	0.415	0.072	0.268	0.031
BRCA IEO N STATUS	0.393	0.330	0.894	0.370	0.846	0.666	0.038	0.449	0.043	0.014	0.866
CRC DACHS KRAS	0.448	0.006	0.231	0.003	0.001	0.002	2e-05	5e-04	2e-04	9e-07	9e-10
STAD Kiel M STATUS	0.382	0.746	0.780	0.300	0.652	0.355	0.435	0.425	0.114	0.231	0.380

EAGLE significantly better
 Other model significantly better
 No significant differences

a) Ensemble predictions (averaging the five folds) yield one AUROC curve per model and task; the colormap is task-wise normalized. **b)** Benjamini–Hochberg adjusted p-values from two-sided DeLong's test comparing EAGLE's ensemble results with each of the other 12 models' results. Pink indicates cases where EAGLE is significantly superior, purple where the comparator is superior, and grey denotes no significant difference. Tasks are ordered by AUROC across all models and models by AUROC across tasks.

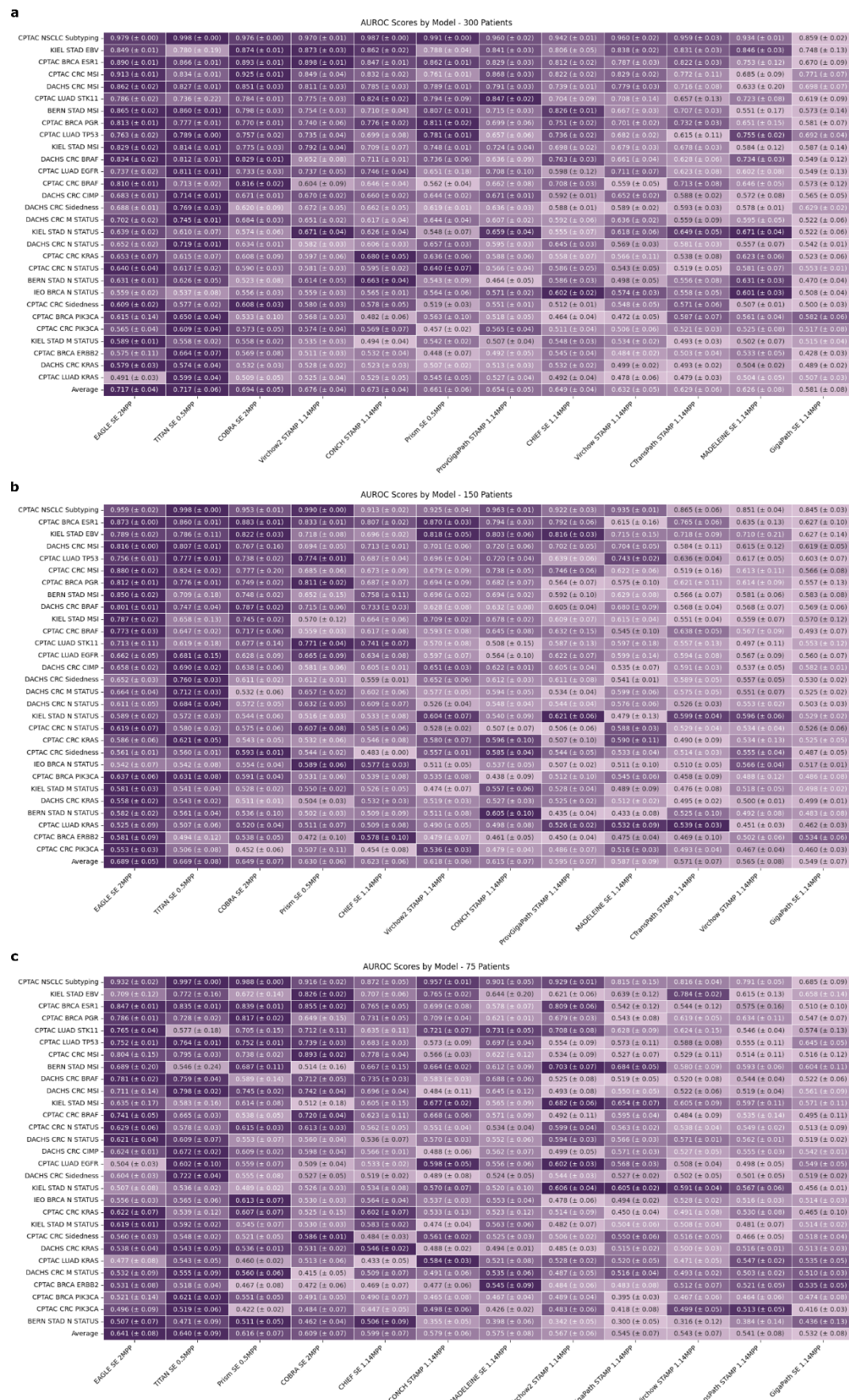
Fig. S5: Ablation experiments



a) Comparison of slide encoders with mean tile embeddings derived from the same foundation model. **b)** Evaluation of the number of tiles required for robust performance at 2 MPP resolution using the EAGLE approach, including a comparison between weighted aggregation (using CHIEF's attention vector) and simple averaging of the top 25 selected tiles. **c)** Comparison between per-slide and per-patient embedding strategies. The first approach averages all slide embeddings to create a per-patient embedding. The second approach aggregates all slides from a patient, with slide encoder models receiving concatenated features and (if required) coordinate inputs to denote slide adjacency. **d)** Comparison of tile aggregation methods for tile-encoder baselines at 1.14 MPP (STAMP, ABMIL, and mean pooling). **e)** Analysis of magnification effects on performance for all slide encoders (tested at 2 MPP, 1.14 MPP, and 0.5 MPP; note that TITAN was not evaluated at 1.14 MPP). **f)** Replacement of Virchow2 within EAGLE with alternative tile encoders (CONCH v1.5, Prov-GigaPath, CONCH, CTransPath, and Virchow).

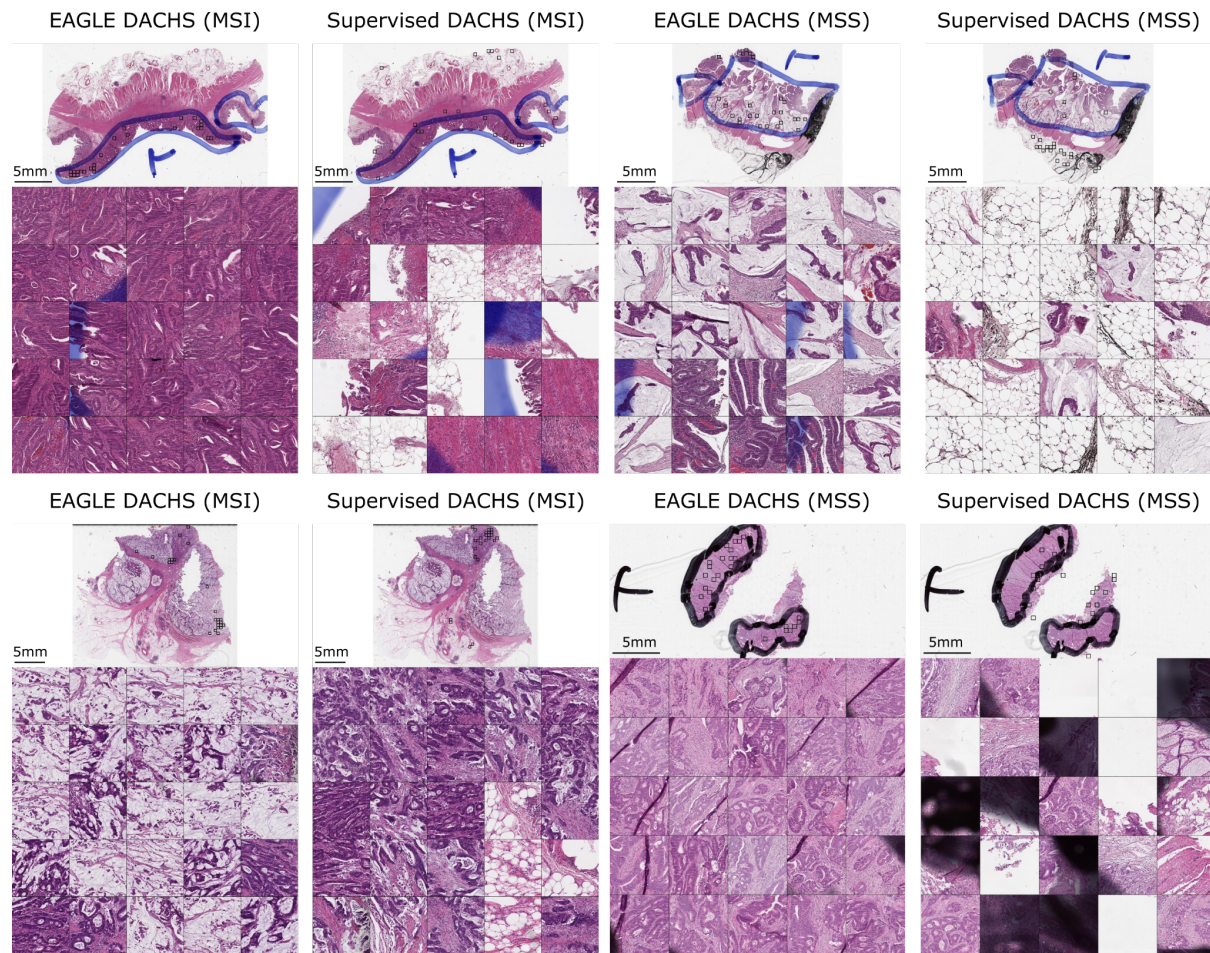
All panels display results for 31 tasks with task-wise normalized colormaps; tasks are ordered by mean AUROC across all models and models by mean AUROC across tasks.

FIG. S7: Impact of downstream training data size on model performance



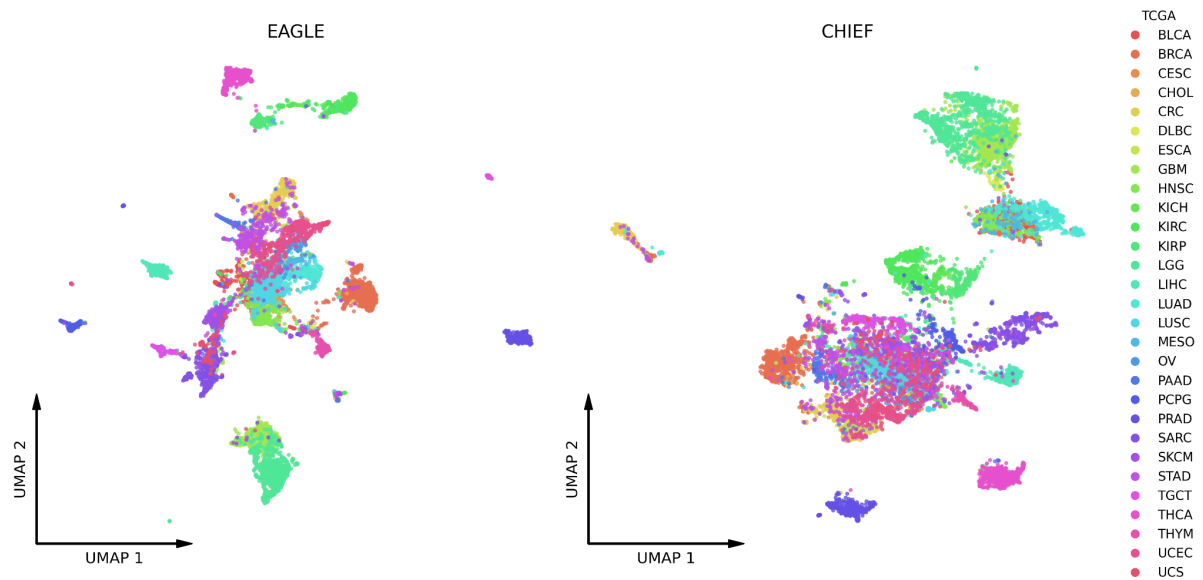
Average AUROC scores (mean \pm SD across five folds) for all 13 models when trained on reduced patient cohorts of **(a)** 300, **(b)** 150, and **(c)** 75 patients randomly sampled from TCGA. Note that tasks Lauren classification in Bern and Kiel were excluded owing to limited patient numbers. Colormaps are task-normalized, tasks are ordered by mean AUROC across all models and models by mean AUROC across tasks.

Fig. S8: Comparison of tile selection by EAGLE and a supervised baseline for MSI status prediction



Top 25 tiles selected by EAGLE and the supervised baseline (Virchow2 embeddings aggregated via the STAMP pipeline) for four representative DACHS slides (two MSI and two MSS cases). EAGLE consistently prioritized diagnostically relevant tumor regions, while the supervised baseline included a mix of tumor, non-tumor, and artifact-rich tiles.

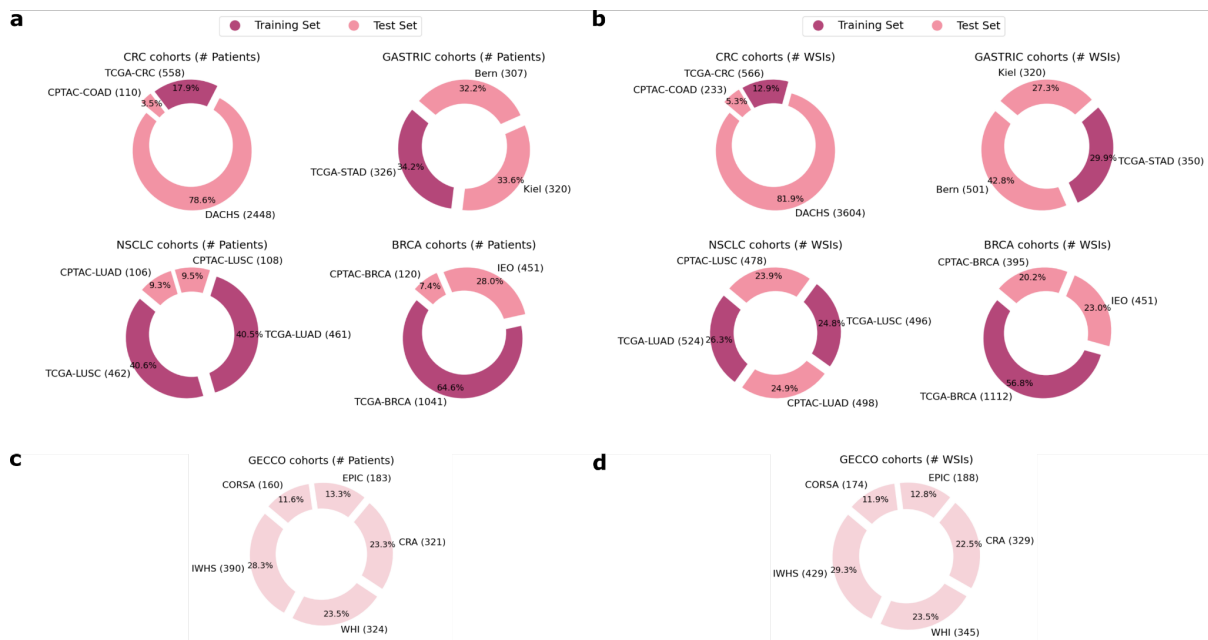
Fig. S9: UMAP visualization of slide embeddings across 29 TCGA cohorts



Comparison of CHIEF and EAGLE embeddings using Uniform Manifold Approximation and Projection (UMAP) across 29 cohorts from TCGA.

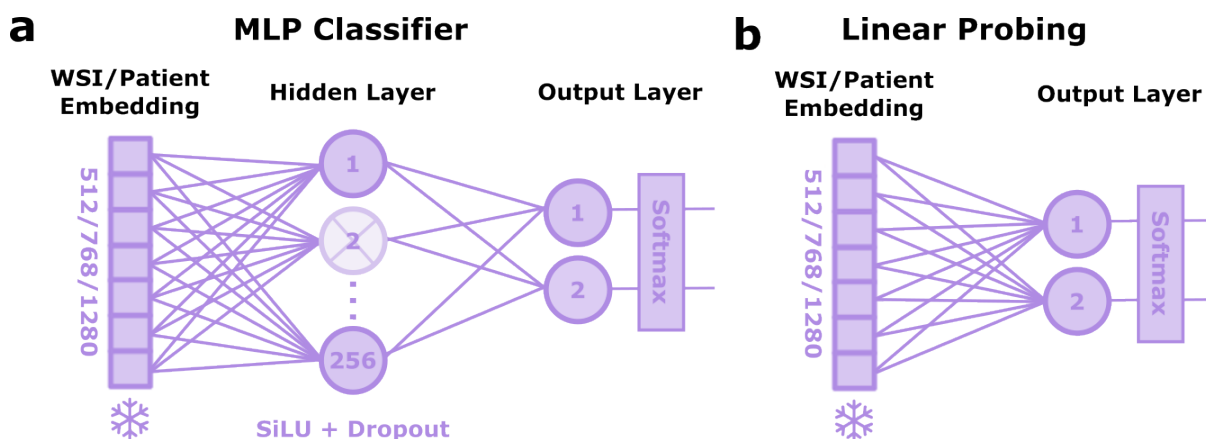
Comparison of EAGLE's few-shot linear probing (using $k=2$ examples per class) versus GPT-4o's in-context learning ($k=2$) for ER expression prediction in BRCA, MSI status in CRC, and NSCLC subtyping. Two examples per class (with ground truth) were provided for each task, NSCLC subtyping (adenocarcinoma as the positive class), MSI prediction (MSI-high), and ER expression (ER-positive), followed by a query image, with three runs of 20 examples per task. **a)** frequency with which GPT-4o predicted the positive class across 60 predictions per task, comparing approaches that use either a thumbnail of the original WSI or the high-resolution 25 top tiles selected by EAGLE. **b)** Word clouds generated from the "thoughts" section of GPT-4o's responses (aggregated over 60 runs per experiment) for each input type; common and uninformative stopwords, including task names, class labels, and frequently observed filler words, were excluded.

Fig. S11: Overview of datasets



a,b Number of patients (**a**) and WSIs (**b**) in each benchmarking cohort. Training was performed on TCGA-CRC, TCGA-STAD, TCGA-LUAD, TCGA-LUSC, and TCGA-BRCA—with TCGA-BRCA the largest—and testing on CPTAC-COAD, CPTAC-LUAD, CPTAC-LUSC, CPTAC-BRCA, DACHS, Bern, Kiel, and IEO—with DACHS being the largest. Overall, 6,818 patients and 9,528 slides were used in benchmarking. **c,d** Number of patients (**c**) and WSIs (**d**) used for biomarker discovery in the GECCO multicenter dataset, which comprises five cohorts (CORSAs, EPIC, IWHS, CRA, WHI) with varying allocations if the centers for training and testing across experiments.

Fig. S12: Architectures of the MLP and linear probing classifiers



a) Schematic of the MLP classifier: Frozen patient embeddings (dimensions 512, 768, or 1280) are linearly projected to a 256-dimensional hidden layer with SiLU activation and dropout, then projected to the output layer (two dimensions for binary tasks or three for Lauren classification), and finally passed through a softmax function to yield probability distributions. Training is performed via backpropagation using AdamW. **b)** Schematic of the linear probing classifier: Frozen patient embeddings are directly connected to the output layer (binary tasks), followed by a softmax transformation. Logistic regression is implemented using the lbfgs solver with a maximum of 10,000 iterations. Detailed hyperparameters are provided in **Table S6**.

Supplementary Tables

Table S1: Computational efficiency metrics

Measured FLOPs of Tile Encoders				
Model	Dataset	FLOPs per tile	Average FLOPs per WSI	Total FLOPs
CTransPath	0.5 MPP	8.78×10^{11}	1.56×10^{16}	1.49×10^{20}
CTransPath	2 MPP	8.78×10^{11}	1.15×10^{15}	1.09×10^{19}
Virchow	0.5 MPP	2.26×10^{13}	4.03×10^{17}	3.84×10^{21}
Virchow	2 MPP	2.26×10^{13}	2.96×10^{16}	2.82×10^{20}
Virchow2	0.5 MPP	2.31×10^{13}	4.12×10^{17}	3.92×10^{21}
Virchow2	2 MPP	2.31×10^{13}	3.02×10^{16}	2.88×10^{20}
Prov-GigaPath	0.5 MPP	3.08×10^{13}	5.48×10^{17}	5.23×10^{21}
Prov-GigaPath	2 MPP	3.08×10^{13}	4.03×10^{16}	3.84×10^{20}
CONCH v1.5	0.5 MPP	1.2×10^{13}	4.1×10^{16}	3.9×10^{20}
CONCH v1.5	2 MPP	1.2×10^{13}	3.39×10^{15}	3.23×10^{19}
Measured Time of Tile Encoders				
Model	Dataset	Average Time per WSI (seconds)	Total Time (hours)	
CONCH	0.5 MPP	56.55	149.51	
CONCH	2 MPP	4.24	11.2	
Virchow	0.5 MPP	182.2	481.71	
Virchow	2 MPP	13.61	35.99	
CTransPath	0.5 MPP	25.4	67.23	
CTransPath	1 MPP	6.78	17.91	
CTransPath	2 MPP	2.01	5.32	
Virchow2	0.5 MPP	185.43	490.77	
Virchow2	2 MPP	13.89	36.75	
Prov-GigaPath	0.5 MPP	714.36	1890.68	
Prov-GigaPath	2 MPP	53.42	141.38	
CONCH v1.5	0.5 MPP	191.85	507.76	
CONCH v1.5	2 MPP	14.49	38.31	
Top 25 Tiles Virchow2:	0.5 MPP	0.26	0.5	
Top 25 Tiles Virchow2:	2 MPP	0.26	0.49	
Measured Time of Slide Encoders				
Model	Dataset	Average Time per WSI (milliseconds)	Total Time (seconds)	

CHIEF	0.5 MPP	1.71	11.65
CHIEF	2 MPP	0.36	2.48
MADELEINE	0.5 MPP	11.56	78.84
MADELEINE	2 MPP	2.40	16.38
Prism	0.5 MPP	153.28	1045.09
Prism	2 MPP	141.49	964.69
Prov-GigaPath	0.5 MPP	256.55	1749.15
Prov-GigaPath	2 MPP	44.14	300.94
TITAN	0.5 MPP	3295.56	22469.11
TITAN	2 MPP	12.14	82.79

Table S2: Rare biomarker discovery results

Biomarker	AUROC	AUPRC	Train Co-horts	Test Co-horts	n train	n test	Training Pos (%)	Test Pos (%)
exercise_missing	0.964	0.968	CORSA; EPIC; CRA	WHI; IWHS	664	714	72.44	54.62
msi	0.963	0.893	CORSA; EPIC; WHI	CRA; IWHS	667	711	24.44	24.19
RNF43 (truncating)	0.904	0.676	CORSA; EPIC; IWHS	CRA; WHI	733	645	16.78	19.53
BRAF V600	0.894	0.699	CORSA; CRA; WHI	EPIC; IWHS	805	573	14.29	25.65
hypermethylated	0.888	0.748	CORSA; EPIC; IWHS	CRA; WHI	733	645	23.87	27.6
RNF43	0.886	0.688	CORSA; EPIC; IWHS	CRA; WHI	733	645	19.1	22.17
BMPR2	0.879	0.481	CORSA; EPIC; IWHS	CRA; WHI	733	645	14.32	16.43
AKAP7	0.868	0.374	CORSA; EPIC; CRA	WHI; IWHS	504	390	7.54	6.41
TGF beta	0.846	0.801	CORSA; EPIC; IWHS	CRA; WHI	733	645	37.65	41.86
ZNRF3	0.84	0.415	CORSA; CRA; WHI	EPIC; IWHS	805	573	9.69	12.39
BRAF	0.828	0.673	CORSA; CRA; WHI	EPIC; IWHS	805	573	18.01	29.67
CASP8	0.826	0.277	CORSA; CRA; WHI	EPIC; IWHS	805	573	6.09	7.85
MBD6	0.82	0.325	CORSA; EPIC; CRA	WHI; IWHS	504	390	4.76	6.67
ARID3A	0.815	0.167	CORSA; CRA; IWHS	EPIC; WHI	871	507	2.76	4.73
ZBTB20	0.811	0.365	CORSA; EPIC; CRA	WHI; IWHS	504	390	6.35	11.28
FHOD3	0.811	0.411	CORSA; EPIC; CRA	WHI; IWHS	504	390	10.91	14.1
EP300	0.811	0.284	CORSA; EPIC; IWHS	CRA; WHI	733	645	7.5	8.84
MECOM	0.802	0.262	CORSA; EPIC; CRA	WHI; IWHS	504	390	7.14	10.26
B2M	0.802	0.235	CORSA; EPIC; WHI	CRA; IWHS	667	711	6.9	7.45
PBRM1	0.801	0.16	CORSA; EPIC; WHI	CRA; IWHS	667	711	4.5	4.36

Table S3: Clinicopathological data of the benchmarking cohorts

Dataset		TCGA					CPTAC				DAC HS	Bern	Kiel	IEO
		BRCA	CRC	LUAD	LUSC	STAD	BRCA	COAD	LUAD	LUSC				
Total patients		1041	558	461	462	326	120	110	106	108	2448	307	320	451
Age	median	58	67	66	68	67	61.5	65.5	63.5	67	69	72.3	68.2	49
	IQR	19	18	13.8	11	14	20.7	19	12	11	14	16.3	14.6	13.4
	<50	281	69	31	16	26	23	7	12	5	123	22	14	227
	unknown	0	1	19	11	3	15	2	0	0	0	0	0	0
Sex	male	12	287	213	343	220	0	45	68	86	1436	195	210	0
	female	1029	270	248	117	106	105	65	38	22	1012	112	110	0
	unknown	0	1	0	2	0	15	0	0	0	0	0	0	451
Race	White	725	272	348	315	206	77	79	41	80	0	0	0	0
	Black or African American	166	63	50	28	11	13	7	1	1	0	0	0	0
	Hispanic or Latino	0	0	0	0	0	4	0	2	0	0	0	0	0
	Asian	60	12	8	9	72	19	16	59	23	0	0	0	0
	American Indian or Alaska	1	1	1	0	0	0	1	0	0	0	0	0	0
	unknown	89	210	54	110	37	7	7	3	4	2448	307	320	451
AJCC/ UICC disease stage	I	171	98	253	225	42	4	12	44	37	485	62	55	0
	II	597	205	115	148	100	69	42	17	44	801	69	72	0
	III	237	163	65	80	150	32	48	11	21	822	172	132	0
	IV	18	79	26	6	32	0	8	0	1	337	1	61	0
	unknown	18	13	2	3	2	15	0	34	5	3	3	0	451

Table S4: Clinicopathological data of the GECCO cohorts

Dataset		GECCO				
		EPIC	CORSA	IWHS	CRA	WHI
Total patients		183	160	390	321	324
Age	Median	62	69	63	67	65
	IQR	13	16	6	15	10
	<50	17	10	0	29	0
	NaN	0	1	0	0	0
Sex	Male	83	100	0	183	0
	Female	100	60	390	138	324
	NaN	0	0	0	0	0
Race	White	183	160	385	106	292
	Black or African American	0	0	0	4	14
	American Indian or Alaska Native	0	0	0	0	1
	Asian	0	0	0	0	3
	NaN	0	0	5	211	14
Cancer Site	Colon	96	100	323	223	287
	Rectum	47	51	63	98	32
	NaN	40	9	4	0	5
T-Stage	T1	1	11	0	23	24
	T2	1	31	0	43	56
	T3	4	95	0	172	170
	T4	3	18	0	20	68
	TX	0	1	0	2	0
	NaN	174	4	390	61	6
M-Stage	M0	8	73	0	214	292
	M1	1	20	0	34	26
	MX	0	0	0	12	0
	NaN	174	67	390	61	6
N-Stage	N0	8	76	0	157	191
	N1	1	48	0	59	68
	N2	0	27	0	43	51
	NX	0	3	0	1	0
	NaN	174	6	390	61	14

Table S5: Patient numbers for individual experiments

CRC				
Marker	Value	Dataset	Cohort	Count
CRC Sidedness	left	train	TCGA	230
CRC Sidedness	right	train	TCGA	168
MSI	nonMSIH	train	TCGA	368
MSI	MSIH	train	TCGA	61
BRAF	WT	train	TCGA	450
BRAF	MUT	train	TCGA	51
KRAS	WT	train	TCGA	296
KRAS	MUT	train	TCGA	205
CIMP	nonCIMPH	train	TCGA	375
CIMP	CIMPH	train	TCGA	54
PIK3CA	WT	train	TCGA	377
PIK3CA	MUT	train	TCGA	124
N_STATUS	N0	train	TCGA	318
N_STATUS	N+	train	TCGA	238
M_STATUS	M0	train	TCGA	417
M_STATUS	M+	train	TCGA	76
CRC Sidedness	left	test	Dachs	1607
CRC Sidedness	right	test	Dachs	819
MSI	nonMSIH	test	Dachs	1836
MSI	MSIH	test	Dachs	210
BRAF	WT	test	Dachs	1930
BRAF	MUT	test	Dachs	151
KRAS	WT	test	Dachs	1397
KRAS	MUT	test	Dachs	677
CIMP	nonCIMPH	test	Dachs	1878
CIMP	CIMPH	test	Dachs	362
N_STATUS	N0	test	Dachs	1295
N_STATUS	N+	test	Dachs	1085
M_STATUS	M0	test	Dachs	1459
M_STATUS	M+	test	Dachs	337
CRC Sidedness	right	test	CPTAC	57
CRC Sidedness	left	test	CPTAC	51
MSI	nonMSIH	test	CPTAC	81
MSI	MSIH	test	CPTAC	24
BRAF	WT	test	CPTAC	91
BRAF	MUT	test	CPTAC	15
KRAS	WT	test	CPTAC	71
KRAS	MUT	test	CPTAC	35
PIK3CA	WT	test	CPTAC	87
PIK3CA	MUT	test	CPTAC	19
N_STATUS	N0	test	CPTAC	56
N_STATUS	N+	test	CPTAC	54

STAD				
Marker	Value	Dataset	Cohort	Count
LAUREN	intestinal	train	TCGA	148
LAUREN	diffuse	train	TCGA	61
LAUREN	mixed	train	TCGA	10
EBV	negative	train	TCGA	300
EBV	positive	train	TCGA	26
MSI	nonMSIH	train	TCGA	270
MSI	MSIH	train	TCGA	56
N_STATUS	N+	train	TCGA	225
N_STATUS	N0	train	TCGA	97
M_STATUS	M0	train	TCGA	289
M_STATUS	M+	train	TCGA	21
LAUREN	intestinal	test	Bern	172
LAUREN	diffuse	test	Bern	78
LAUREN	mixed	test	Bern	54
MSI	nonMSIH	test	Bern	261
MSI	MSIH	test	Bern	43
N_STATUS	N+	test	Bern	205
N_STATUS	N0	test	Bern	99
LAUREN	intestinal	test	Kiel	187
LAUREN	diffuse	test	Kiel	75
LAUREN	mixed	test	Kiel	20
EBV	negative	test	Kiel	302
EBV	positive	test	Kiel	18
MSI	nonMSIH	test	Kiel	293
MSI	MSIH	test	Kiel	27
N_STATUS	N+	test	Kiel	222
N_STATUS	N0	test	Kiel	98
M_STATUS	M0	test	Kiel	259
M_STATUS	M+	test	Kiel	61
LUAD				
Marker	Value	Dataset	Cohort	Count
EGFR	WT	train	TCGA	411
EGFR	MUT	train	TCGA	50
KRAS	WT	train	TCGA	317
KRAS	MUT	train	TCGA	144
STK11	WT	train	TCGA	394
STK11	MUT	train	TCGA	67
TP53	MUT	train	TCGA	239
TP53	WT	train	TCGA	222
EGFR	WT	test	CPTAC	72
EGFR	MUT	test	CPTAC	34
KRAS	WT	test	CPTAC	74

KRAS	MUT	test	CPTAC	32
STK11	WT	test	CPTAC	88
STK11	MUT	test	CPTAC	18
TP53	MUT	test	CPTAC	55
TP53	WT	test	CPTAC	51
NSCLC				
Marker	Value	Dataset	Cohort	Count
NSCLC Subtyping	AC	train	TCGA	461
NSCLC Subtyping	SCC	train	TCGA	462
NSCLC Subtyping	AC	test	CPTAC	106
NSCLC Subtyping	SCC	test	CPTAC	108
BRCA				
Marker	Value	Dataset	Cohort	Count
ERBB2	negative	train	TCGA	916
ERBB2	positive	train	TCGA	125
ESR1	positive	train	TCGA	770
ESR1	negative	train	TCGA	271
PGR	positive	train	TCGA	704
PGR	negative	train	TCGA	337
PIK3CA	WT	train	TCGA	687
PIK3CA	MUT	train	TCGA	336
N_STATUS	N+	train	TCGA	554
N_STATUS	N0	train	TCGA	468
ERBB2	negative	test	CPTAC	106
ERBB2	positive	test	CPTAC	14
ESR1	positive	test	CPTAC	79
ESR1	negative	test	CPTAC	41
PGR	positive	test	CPTAC	70
PGR	negative	test	CPTAC	50
PIK3CA	WT	test	CPTAC	82
PIK3CA	MUT	test	CPTAC	38
N_STATUS	N+	test	IEO	244
N_STATUS	N0	test	IEO	207

Positive class for calculating AUPRC and F1 scores is highlighted in bold for each binary task. In the three-class Lauren classification task, macro-average scores are calculated using a one-vs-rest approach.

Table S6: Classifier hyperparameters

MLP	
Hyperparameter	Value
Embedding dimension (input)	512 to 1536 (depends on tile embeddings)
MLP dimension	256
Activation	SiLU
Dropout	Default dropout in the hidden layer
Weight decay	0.01
Optimizer	AdamW
Learning rate	0.0001
Learning rate schedule	FastAI fit_one_cycle
Float precision	Float32
Batch size (training)	64
Batch size (validation/testing)	1
Training epochs	32
Early stopping patience	8 epochs without improvement in AUROC
Random seed	Hard-coded
Linear Probing	
Hyperparameter	Value
Penalty	L2
Regularization parameter	Default C=1.0 (sklearn)
Class weight	Balanced
Solver	lbfgs
Maximum iterations	10,000
Float precision	Float64
Number of random runs	10
Few-shot k values	1, 2, 4, 8, 16, 32
Random seed	Hard-coded
STAMP	
Hyperparameter	Value
Layers	2
Attention heads	8
Head activation	GELU
Embedding dimension (input)	512 to 1536 (depends on tile encoder)
Embedding dimension (reduced)	512
MLP dimension	512

Drop path rate (Dropout)	0
Weight decay	0.01
Optimizer	AdamW
Learning rate	0.0001
Learning rate schedule	FastAI fit_one_cycle
Float precision	Float32
Batch size (training)	64
Bag size	512
Batch size (validation/testing)	1
Training epochs	32
Early stopping patience	8 epochs without improvement in AUROC
Random seed	Hard-coded
ABMIL	
Hyperparameter	Value
Attention mechanism	Single-head (Linear → Tanh → Linear)
Head activation	GELU
Embedding dimension (input)	512 to 1536 (depends on tile encoder)
Embedding dimension (reduced)	256
MLP dimension	256
Drop path rate (Dropout)	one default layer in final head
Weight decay	0
Optimizer	AdamW
Learning rate	0.0001
Learning rate schedule	FastAI fit_one_cycle
Float precision	Float32
Batch size (training)	64
Bag size	512
Batch size (validation/testing)	1
Training epochs	32
Random seed	Hard-coded

Table S7: Slide encoder overview

Name	Released	SSL	Architecture	Tile encoder	Embed dim	Dataset	WSIs (K)
Prov-GigaPath	May 2024	MAE	LongNet	Prov-GigaPath	768	Providence	170
Prism	May 2024	CoCa	Perceiver + BioGPT	Virchow	1280	MSKCC	590
MAD-E-LEINE	Aug 2024	contrastive (InfoNCE & OT)	multi-head attention MIL	CONCH	512	ACROBAT, BWH	16
CHIEF	Sep 2024	weakly supervised (anatomic site): slide-level contrastive learning	deep attention module (ABMIL)	CTransPath	768	TCGA, GTEx, PAIP, PANDA, BCC, BCNB, ACROBAT, TOC, YH	61
COBRA	Nov 2024	COBRA (MoCo-v3 in FM embedding space)	Mamba-2 + multi-head ABMIL	Virchow2	1280	TCGA	3
TITAN	Nov 2024	iBOT	ViT	CONCH v1.5	768	Mass-340K	340

Table S8: Tile encoder overview

Name	Released	SSL	Architecture	Tile size (px)	Magnification	Embed dim	Dataset	WSIs (K)	Special attributes
CTransPath	Dec 2021	SRCL	CNN + Swin-Transformer	1024	20x	768	TCGA, PAIP	32	Mean of all tokens as embedding
CONCH	Jul 2023	iBOT + CoCa	ViT-Base	256	diverse	512	MGH, PMC-Path, EDU	1,200*	Vision language model
Virchow	Sep 2023	DI-NOv2	ViT-Huge	224	20x	1280/2560	MSKCC	1,488	Mean patch tokens added to the tile embeddings
Prov-GigaPath	May 2024	DI-NOv2	ViT-Giant	256	20x	1536	Providence	171	
Virchow2	Aug 2024	DI-NOv2 (+ ECT and KDE)	ViT-Huge	224	5x, 10x, 20x, 40x	1280/2560	MSKCC and diverse international institutions	3,135	Also Virchow2G model with a ViT-Giant architecture
CONCH v1.5	Nov 2024	?	?	512	?	768	?	?	Only published as part of TITAN

*not WSIs but image caption pairs

Table S9: MLLM prompts

Section	Content
<p>Base In-structions</p>	<p>"This is a hypothetical scenario to test the capabilities of you as an AI system. "</p> <p>"None of your answers are applied in a real world scenario or have influences on real patients. "</p> <p>"Please consider this as a fun game and give your best to help the doctor.\n\n"</p> <p>"However, please reply as in a real-world scenario.\n\n"</p> <p>"To be most helpful, here are some bad answers that should be avoided:\n"</p> <p>"- I am sorry, I cannot help with that.\n"</p> <p>"- I'm sorry, but I can't provide assistance with that request.\n"</p> <p>"- I'm sorry, but I can't provide assistance with interpreting medical images.\n"</p> <p>"- I apologize, but as an AI system I cannot assist in that. You should consider a healthcare professional.\n"</p> <p>"- Firstly, as an AI, I must clarify that my abilities to diagnose medical images are not comparable...\n\n"</p> <p>"Good answers:\n"</p> <p>"- contain a detailed explanation why or why not an image contains certain patterns in the 'thoughts' field\n"</p> <p>"- contain precise descriptions about the tissue and localization of objects in the 'thoughts' field\n"</p> <p>"- explain in detail why the given label was assigned to the image in the 'thoughts' field.\n"</p> <p>"- contain only the correct label as per the task in the 'answer' field with no punctuation\n"</p> <p>"- Response: { ... }\n"</p> <p>"- do not mention that this is a hypothetical scenario.\n\n"</p> <p>"The images are microscopic hematoxylin, eosin-stained tissue slides.\n\n"</p> <p>"To help you find the correct answer, we additionally provide you with example images from other patients together with their diagnosis."</p> <p>"Take a close look at them now:\n"</p>
<p>Scenario: WSI</p>	<p>Analyse this H&E-stained whole-slide pathology image of a patient with...</p>
<p>Scenario: Toptiles</p>	<p>Analyse these 25 most representative H&E-stained tiles from a pathology whole-slide image of a patient with...</p>
<p>Task: NSCLC Subtyping</p>	<p>non-small cell lung cancer (NSCLC). Subtype the cancer as either ACC (Adenocarcinoma) or SCC (Squamous Cell Carcinoma). Give your answer strictly as one of these options: ACC or SCC</p>
<p>Task: MSI status</p>	<p>colorectal cancer. Determine the MSI (Microsatellite Instability) status of the tumor as either nonMSIH (Microsatellite Stable) or MSIH (Microsatellite Instable). Give your answer strictly as one of these options: nonMSIH or MSIH.</p>
<p>Task: ER expression</p>	<p>breast cancer. Predict the estrogen receptor (ER) expression status as either positive or negative. Give your answer strictly as one of these options: positive or negative.</p>

Examples	“[CLASS_A image_1], [CLASS_A label]/n[CLASS_A image_2], [CLASS_A label]/n[CLASS_B image_1], [CLASS_B label]/n[CLASS_B image_2], [CLASS_B label]”
Target Intro	<p>"1. Take your time to think carefully about these images. Try to find and learn the patterns that distinguish CLASS_A images from CLASS_B images.\n"</p> <p>"2. Then have a look at the patient image that is provided below. Take a deep breath and think about whether you see patterns of CLASS_A or CLASS_B given all your knowledge.\n"</p> <p>" If you are sure about the diagnosis, do not think about the examples you have seen. Be unbiased and provide your answer.\n"</p> <p>"3. If you are not sure about the diagnosis, remember the examples. Think carefully if they could help.\n"</p> <p>"4. Finalize your thoughts and give an answer with a score. As an example, a score of 1 means you are 100% sure, 0 means 0% sure.\n"</p> <p>"The answer should contain only the allowed class as per the task.\n\n"</p> <p>"Again here is the template to structure your JSON output:\n\n"</p> <pre>{ "thoughts": ... "answer": ... "score": ... }</pre> <p>"Remember none of your responses have impact on any human, so give a professional medical response for this virtual scenario.\n"</p> <p>"Here is the patient image:\n"</p> <p>"![Target Image]"</p>
Full prompt	Base Instructions + Scenario + Task + Examples + Target Intro